Predicting moisture condensation risk on the radiant cooling floor of an office using integration of a genetic algorithm-back-propagation neural network with sensitivity analysis

Meng Su [a], Jiying Liu [a,*], Moon Keun Kim [b], Xiaozhou Wu [c]

[a] School of Thermal Engineering, Shandong Jianzhu University, Jinan 250101, China

[b] Department of Civil Engineering and Energy Technology, Oslo Metropolitan University, Oslo N-0130, Norway

[c] School of Civil Engineering, Dalian University of Technology, Dalian, China

ARTICLE INFO

ABSTRACT

Pre-dehumidification time (τ_{pre}) and pre-dehumidification energy consumption (E_{pre}) play important roles in preventing the condensation of moisture on the floors of rooms that use a radiant floor cooling (RFC) system. However, there are few theoretical or experimental studies that focus on these two important quantities. In this study, an artificial neural network (ANN) was used to predict condensation risk for the integration of RFC systems with mixed ventilation (MV), stratum ventilation (SV), and displacement ventilation (DV) systems. A genetic algorithm-back-propagation (GA-BP) neural network model was established to predict τ_{pre} and E_{pre}. Both training data and validation data were obtained from tests in a computational fluid dynamics (CFD) simulation. The results show that the established GA-BP model can predict τ_{pre} and E_{pre} well. The coefficient of determination (R^2) of τ_{pre} and of E_{pre} were, respectively, 0.973 and 0.956. For an RFC system integrated with an MV, SV, or DV system, the lowest values of τ_{pre} and E_{pre} were with the DV system, 23.1 s and 0.237 kWh, respectively, for a 67.5 m^3 room. Therefore, the best pre-dehumidification effect was with integration of the DV and RFC systems. This study showed that an ANN-based method can be used for predictive control for condensation prevention in RFC systems. It also provides a novel and effective method by which to assess the pre-dehumidification control of radiant floor surfaces.

1. Introduction

Global warming increasingly affects people's health and quality of life [1,2]. Among the countries of the world, China has been the largest carbon emitter and energy consumer since 2011 [3,4]. In general, building energy is used mainly for lighting, electrical devices, and heating, ventilating, and air conditioning (HVAC) systems, of which about 50% are traditional HVAC systems [5]. People are advocating low-carbon lifestyle while pursuing a higher quality of life as the concept of energy saving and emission reduction has become popular [6,7]. The application of energy-saving technology in HVAC systems is one important means by which to slow the upward trend of energy consumption [8,9].

Radiant-cooling air conditioning systems make use of enclosing surfaces as cooling sources to exchange heat with humans by way of radiation and convection [10–12]. A radiant cooling system can maintain the same human thermal comfort as a conventional convective air conditioning system with an indoor temperature 1 to 2 K higher than for a conventional system [13,14]. Also, radiant cooling systems can be characterized as having uniform indoor-temperature distribution, ideal thermal comfort, quiet operation, and energy saving. [15,16]. Accordingly, radiant cooling systems are gaining favor and have also become the focus of study by researchers in the HVAC field [17,18]. At the same time, however, there are some disadvantages such as high initial cost, inability to dehumidify the air, the possibility of water vapor condensation, and a relatively long start-up time [19,20].

The biggest challenge in using radiant cooling is the risk of moisture condensation on the surface of chilled radiant plates (floors, ceiling or walls) [21,22]. Condensation occurs most likely in two situations: an

---

Nomenclature

$E_{chiller}$	energy consumption of the chiller (kWh)
E_{fan}	energy consumption of the fan (kWh)
E_{pre}	pre-dehumidification energy consumption (kWh)
H_{as}	air supply humidity ratio (g/kg)
Q	cooling load of conditioning the outdoor fresh air to the air supply state (kWh)
T_{as}	air supply temperature (˚C)
T_{floor}	floor temperature (˚C)
T_{ini}	initial indoor air temperature (˚C)
V_{as}	air supply flow rate (m^3/s)
V_m	different ventilation mode

Greek letters

β	thermal expansion factor (1/K)
ε	turbulent dissipation rate (m^2/s^3)
μ	dynamic viscosity (N·s/m^2)
ρ	air density (kg/m^3)
τ_{pre}	pre-dehumidification time (h)
η	efficiency
η_{fan}	fan efficiency

Subscripts

as	air supply
chiller	chiller device
floor	radiant floor
fan	fan device
ini	initial indoor air
m	mode
out	outdoor air
pre	pre-dehumidification

increase in indoor air dew point temperature (DPT) due to air infiltration from open windows and doors or significant internal moisture gain from the occupants [23]. When such a situation prevails, adjusting the temperature of the chilled water or cutting off the chilled water supply can prevent condensation [24]. In addition, condensation occurs at the start-up moment of a radiant cooling system, usually in the morning, because the indoor air moisture level is higher after a night's accumulation while the temperature of chilled water entering the radiant panels is low. Supplying fresh air to bear the indoor latent load and partial cooling load is a good choice for solving the problem of condensation [25]. Moreover, it plays an important role in improving energy efficiency and indoor thermal comfort [26].

Most non-residential buildings have regular occupancy hours, which are called occupied times. After these hours or on weekends, the spaces in these building are not used; these are unoccupied times [27]. An effective approach is to operate ventilation systems during the unoccupied times before operating radiant cooling systems during the occupied times.

Most recent studies on the prevention of condensation in these two situations have focused on radiant ceiling cooling (RCC) [28–30], while radiant floor cooling (RFC) has received more limited attention, especially condensation occurs at the start-up moment. Lim et al. [31] conducted numerical simulations and experimental tests to study control methods for RFC air-conditioning systems in Korean residential buildings. Their results showed that for room temperature control, indoor- and outdoor-temperature-feedback-based water temperature control was superior to water flow rate control and could effectively control condensation. Ren et al. [32] used a measurement method to study the operational control of RFC with displacement ventilation (DV) systems. A recommendation was to implement a 1–1.5 h start of the DV system for dehumidification before the occupied time, when condensation on the radiant surface can be effectively prevented.

Based on the climate characteristics of Hong Kong, Zhang and Niu [33] suggested that turning on a ventilation system one hour before starting a radiant cooling system can effectively prevent radiant panel condensation.

When comparing ventilation strategies [34], a DV system is regarded as one of the most interesting solutions, because it can provide a high level of air quality at the breathing level [35,36]. Consequently, there have been many studies of the combination of a DV system and an RFC system [32,35]. In contrast, the applications of mixed ventilation (MV) and stratum ventilation (SV) systems have been investigated only in limited studies. Liu et al. [37] evaluated the thermal comfort performance of RFC systems when combined with different ventilation systems. The conclusion was that MV and SV systems have small vertical air temperature gradients and better thermal comfort. Li et al. [38] found that an SV system can effectively control air pollutants and provide better thermal performance, thermal comfort, and indoor air quality. Most of the published studies are focused on air quality and indoor thermal comfort [39,40]; there are relatively few studies on the integration of RFC with different ventilation systems for pre-dehumidification.

The start time of a ventilation system before the room is occupied—that is, the pre-dehumidification time (τ_{pre})—is critical. It influences both pre-dehumidification energy consumption (E_{pre}) and the prevention of condensation. The longer is τ_{pre}, the better the effect of condensation prevention. However, most energy is consumed in handling and delivering the outdoor air. In practical application, it is quite hard to determine the optimal building design and HVAC system operation in relation to τ_{pre} and E_{pre} due to the large number of variables that need to be considered [41].

Artificial neural networks (ANNs) are widely accepted for overcoming the limitations of physical modeling of complicated systems and processes [42]. They have been used by many researchers for predictive control of building systems. Ruano et al. [43] discussed the design of indoor air temperature prediction using an ANN model. Ben-nakhi et al. [44,45] used ANN to optimize the thermal behavior of air conditioning in office buildings and public buildings. The end time of thermostat failure and the cooling load of buildings were predicted for saving energy. Yang et al. [27,46] used ANN to predict the time of indoor air temperature drop and to realize the start and stop control of indoor heating system. The above results show that a predictive control method using ANN is effective and has high accuracy.

At present, ANN techniques have been applied by a number of researchers for modeling and predicting radiant cooling-system ventilation and dehumidification. Ge et al. [25] used ANN to predict the risk of condensation on cooling ceilings and to predict the optimum τ_{pre}. They used two ANN models to predict the temperature of the cooling ceiling and indoor air DPT when the system is started. A third model was also used to predict the optimum τ_{pre} for a condensation-prevention system. The results showed that for buildings in Hong Kong, 30 min of pre-dehumidification time is sufficient. Keblawi et al. [47] studied a model-based RCC and DV online monitoring system, established a dynamic multi-variable cost function, and used a genetic algorithm (GA) to solve the problem. Their results showed that online optimization control produced good results and could improve the energy efficiency of RCC and DV systems.

Since the training of a neural network requires a large amount of data, most recent studies have focused on the application of a transient system simulation program (TRNSYS) to obtain the needed amount of data [25,48]. In recent decades, the CFD method has been demonstrated to be a highly efficient tool in the design of indoor environments and planned energy consumption [49]. Because air distribution in a room directly affects the ventilation and air conditioning, the use of TRNSYS cannot yield detailed distribution of the air in a space. Compared with experimental studies, CFD is characterized by lower costs, and the detailed indoor air distribution can be more accurately predicted than with
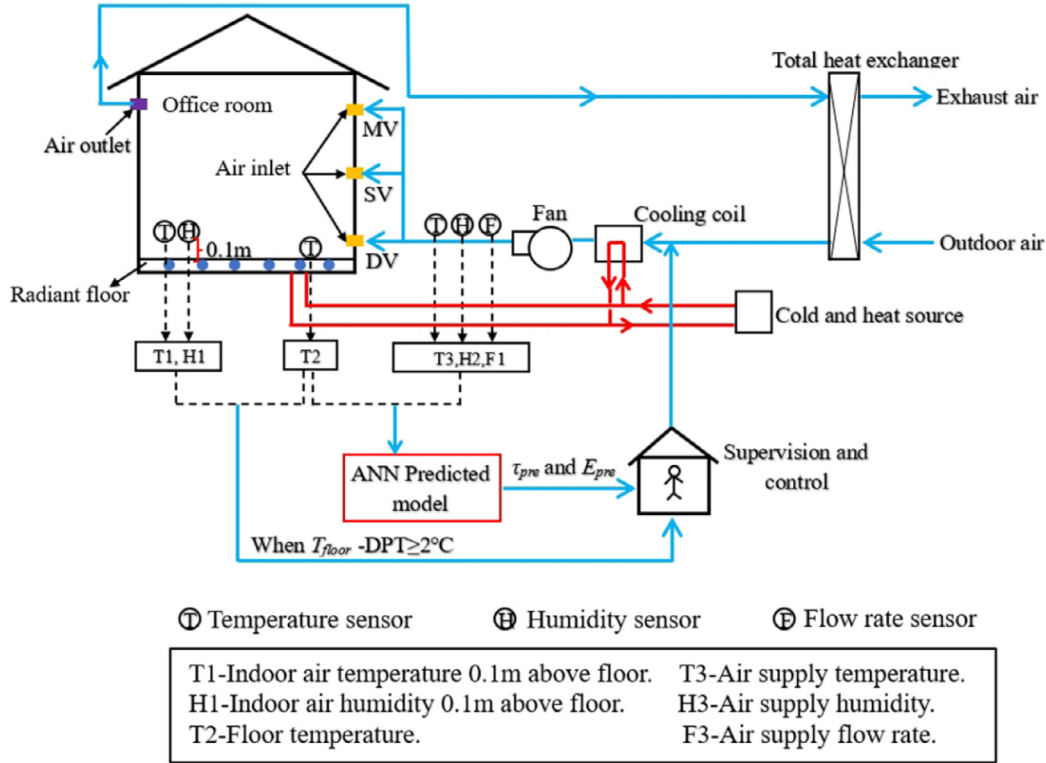
Fig. 1. Schematic of RFC integrated with a DV, SV, or MV system and ANN prediction model for dehumidifying an indoor thermal environment.

TRNSYS. This study therefore used a CFD simulation to obtain some numerical results, followed by the neural network method for training and prediction.

As an advanced neural network model in computer processing, pattern recognition, and data analysis with good corrections, the back propagation (BP) neural network follows a multi-layer feed-forward neural network with error, which has been widely used to simulate numerical data analysis and to predict pattern recognition and intelligent control [50]. Although the BP neural network has high accuracy, it still has some defects [51]. For example, when the initial value is not appropriate, it has some errors, and the topological structure is not comprehensive. Because of these limitations, this study used GA to improve the BP neural network and achieve higher accuracy.

Aiming at the problem of pre-dehumidification, the RFC environment integrated with different ventilation systems is established. Fig. 1 shows a schematic of RFC integrated with a DV, SV, or MV system and ANN predicted model for dehumidification control of an indoor thermal environment. The main principle is to transmit the temperature, humidity, and flow rate sensor data to the ANN prediction model to obtain τ_{pre}, so that management can know how long to ventilate before turning on the RFC system. After the RFC system is turned on, the difference between the DPT and the floor temperature can be monitored to determine whether ventilation parameters need to be changed to avoid condensation on the floor surface. However, the key to control is whether an ANN model can provide accurate prediction. Therefore, the goal of this study is to establish a good ANN prediction model for future pre-dehumidification control. The ANSYS Fluent 16.2 software was used to simulate the thermal and humidity environments of an office located in Jinan, China, in the summer. τ_{pre} and E_{pre} were set as the predicted target parameters. Different modes of ventilation (V_m), air-supply temperature (T_{as}), air-supply humidity ratio (H_{as}), air-supply flow rate (V_{as}), and floor temperature (T_{floor}) were used as design variables. Finally, the influence of different design parameters on τ_{pre} and E_{pre} were analyzed based on CFD simulation and the algorithm-back-

propagation (GA-BP) prediction model for predicting τ_{pre} and E_{pre} was obtained.

2. Research methodology

2.1. Description of the geometric model

A typical office room was chosen as the study object of the simulation analysis; its size was $6.0\ m \times 4.5\ m \times 2.5$ m. The heat sources consisted of two office workers, each providing a heat flux of 147 W; two computers, each providing a heat flux of 370 W; and a 40-W lamp located near the ceiling. The air supply opening heights of DV, SV, and MV systems were 0.1, 1.15, and 2.2 m, respectively. The outlet was close to the ceiling. The size of the inlet was $0.2\ m \times 0.8$ m and of the outlet $0.2\ m \times 0.25$ m. Fig. 2 shows an isometric view of the simulation model. The detailed configuration of this model is provided in Table 1.

2.2. Numerical model and schemes

This study first conducted the simulation using commercial CFD software, namely ANSYS Fluent 16.3. Different ventilation systems combined with the RFC system were applied using the Boussinesq approximation due to the effect of air density differences. The turbulent flow was assumed and an incompressible gas composed of dry air and water vapor was chosen. Previous studies [52,53] revealed that the renormalized group RNG k-ε turbulence model produces an accurate prediction of indoor air flow and temperature. For the pressure-velocity coupling, the semi-implicit method for pressure-linked equations (SIMPLE) algorithm was selected. Pressure staggering option (PRESTO!) discretization was specified for the pressure solution. The second-order upwind scheme was applied to momentum, energy, turbulent kinetic energy, and turbulent dissipation rate. The details of the numerical model and simulation setup are summarized in Table 2.

ARTICLE IN PRESS

JID: ENBENV [m5GeSdc;September 7, 2022;18:55]

M. Su, J. Liu, M.K. Kim et al. Energy and Built Environment xxx (xxxx) xxx
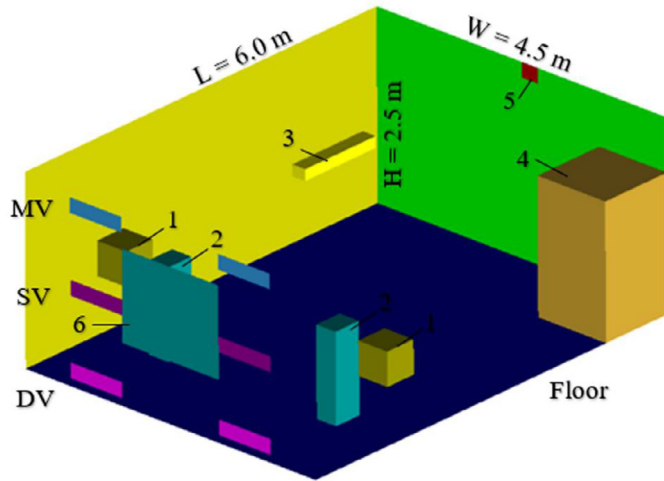
Fig. 2. Isometric view of the CFD simulation. (DV: displacement ventilation; SV: stratum ventilation; MV: mixed ventilation. 1-computer; 2-human model; 3-lamp; 4-bookcase; 5-air outlet; 6-window.).

Table 1
Configuration of the simulation model.

Component	Description	Number
DV	Air inlet size 0.8 m × 0.2 m, air supply opening height 0.1 m	2
	Air outlet size 0.25 m × 0.2 m	1
SV	Air inlet size 0.8 m × 0.2 m, air supply opening height 1.15 m	2
	Air outlet size 0.25 m × 0.2 m	1
MV	Air inlet: 0.8 m × 0.2 m, air supply opening height 2.2 m	2
	Air outlet size 0.25 m × 0.2 m	1
Human model	Dimensions 0.4 m × 0.3 m × 1.2 m, cooling load 147 W, moisture 109 g/h	2
Computer	Dimensions 0.45 m × 0.45 m × 0.45 m, cooling load 370 W	2
Lamp	Dimensions 1.2 m × 0.2 m × 0.15 m, cooling load 40 W	1
Window	Dimensions 1.5 m ×1.2 m	1
Bookcase	Dimensions 1.05 m × 0.4 m ×1.8 m	1

2.3. Setting up boundary condition

For an office building, as noted above, there is a fixed time of use, called occupied time. The RFC system is opened when the space is occupied, but the rate of T_{floor} cooling is slow, and due to the moisture added by the human body, the air DPT near the floor will gradually increase and soon become greater than T_{floor}, causing condensation. Therefore, it is necessary to open the ventilation system to reduce the DPT near the floor to an ideal level in the unoccupied time. In this study, the ideal level for opening the RFC system was chosen to be when DPT was 2 °C lower than T_{floor}. Fig. 3 shows the DPT curve in the room during occupied and unoccupied time, as well as the variation of ventilation system
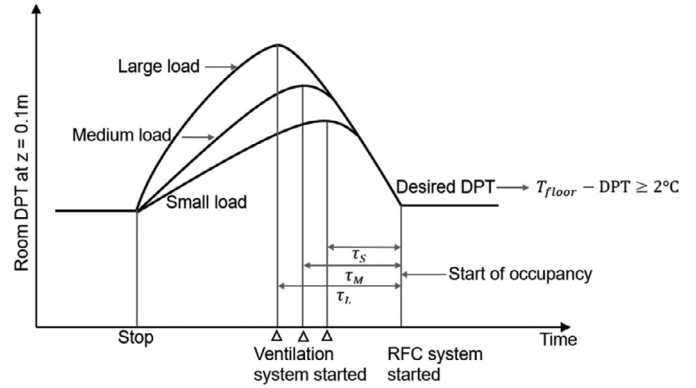

Fig. 3. DPT as a function of time at $z = 0.1$ m for several load conditions [27].

Table 3
The setting-up initial indoor parameters at different floor temperature.

T_{floor} (°C)	T_{ini} (°C), H_{ini} (%)	DPT (°C)
20	26, 65.02	19
21	26.5, 67.21	20
22	27, 69.44	21

start-up time with cooling load. With an increase of cooling load, the start-up time (τ_L, τ_M, or τ_S) of the ventilation system must come earlier. If the ventilation time before the occupied time is too long, energy will be wasted; if it is too short, DPT will not have reached the ideal level when the space is occupied, which will lead to condensation on the floor. To reach an ideal level, an optimal start time is needed. However, since τ_{pre} and E_{pre} are related not only to air supply parameters and operation, but also to the mode of ventilation, five factors affecting the τ_{pre} and E_{pre} are considered: V_m, T_{as}, H_{as}, V_{as}, and T_{floor}.

The selected V_{as} were set as 0.016, 0.024, and 0.036 m^3/s in order to fulfill summer conditions and satisfy the recommended outdoor ventilation rate [54]. In addition, T_{as} should be at least 2 °C lower than the indoor air temperature [55]. Therefore, the calculated T_{as} values were selected to be 21, 22, and 23 °C, and the predefined H_{as} values were set as 6.5, 7.25, and 8 g/kg. When the RFC system is open, T_{floor} should be larger than 18 °C so the air supply can efficiently spread along the floor at T_{floor} below 25 °C [56].

Therefore, the values of T_{floor} in the simulation were selected as 20, 21, and 22 °C. The difference between T_{floor} and DPT was set as 1 °C. The setting-up initial indoor temperature (T_{ini}) and relative humidity (H_{ini}) at different values of T_{floor} are shown in Table 3. Based on these choices, the selected values of different influencing factors are listed in Table 4. A selection of simulation parameters was chosen to obtain 243 data sets of the five variables in different combinations. The personnel and equipment cooling were ignored, as there was no occupant in the numerical simulation of pre-dehumidification. In addition, the predefined outdoor air temperature was set as 32 °C and the outdoor the relative humidity as 85%.

Table 2
Numerical model and simulation setup.

Solver	3D pressure based, transient state, implicit formulation
Turbulence model	RNG k-ε turbulence model
Species model	Species transport
Numerical schemes	For pressure, the staggered third scheme PRESTO!; for other terms, second-order upwind discretization scheme and the SIMPLE algorithm
Air inlet	Velocity inlet
Air outlet	Pressure outlet
Floor, ceiling, window, side walls	Constant-temperature surfaces
bookcase	Adiabatic surface

Table 4
The setting-up variables for different simulation cases.

Variable	Selected values	Unit
V_m	DV, SV, MV	-
V_{as}	0.016, 0.024, 0.032	m³/s
T_{as}	21, 22, 23	°C
H_{as}	6.5, 7.25, 8	g/kg
T_{floor}	20, 21, 22	°C

2.4. Energy consumption calculation

This study mainly focused on the pre-dehumidification stage while the radiant floor system was shut off. Therefore, the energy consumption generated by cooling coils in order to eliminate the heat load of the indoor space is not included in the calculation of cooling energy consumption. Only the portion of cooling energy used to condition the outdoor fresh air to the air supply state is included. The total cooling load Q, which is the energy portion used to condition the outdoor fresh air (kW), can be expressed by Eq. (1) below [57]. The energy consumption equipment in the operation of ventilation system includes fan and chiller. Its power is calculated using Eqs. (2) and (3) below [58].

$$Q = V_{as}\rho(h_{out} - h_{as})\tau_{pre} \qquad (1)$$

where V_{as} is the air supply flow rate (m³/h), ρ is air density, the value of which was taken to be 1.29 kg/m³, and h_{out} and h_{as} are, respectively, the specific enthalpies of the outdoor and supply air. The energy consumption of the fan (kWh) is

$$E_{fan} = \frac{V_{as}\Delta p}{3600\eta_{fan}}\tau_{pre} \qquad (2)$$

where Δp is the fan total pressure rise (Pa), and η_{fan} is the fan efficiency. The energy consumption of the chiller (kWh) is

$$E_{chiller} = \frac{Q}{COP} \qquad (3)$$

where COP (the coefficient of performance) is the ratio of the cooling power to the electricity input power.

2.5. Grid independence analysis

In order to study the grid independence of simulation, the numerical results of temperature and humidity variation at $z = 0.1$ m for three different grids were compared. There are 337,542, 529,276, and 836,336 cells in coarse, medium, and fine grids. Fig. 4 shows differences in temperature and humidity for different grids. Fig. 4(a) shows temperature vs. time, with the blue area showing differences between coarse and medium grids, and the red area showing differences between medium and fine grids. It can be seen from the figure that the blue area fluctuates significantly, indicating that the errors between coarse and medium grids are large, the maximum difference reaching 0.084 °C. The red area shows less fluctuation, with a small difference only after 60 s, and a maximum difference of 0.058 °C. The same trends show up also in the humidity comparison of Fig. 4(b), where the blue area fluctuates significantly, with a maximum difference of 0.198 g/kg, while the red area fluctuates only slightly, with a difference of 0.093 g/kg, less than the difference from medium to fine grid by about 53%. Therefore, the medium grid size with 529,276 cells was selected for the subsequent numerical simulation study.

2.6. Model validations

To verify the accuracy of the simulation model established in this study, Ma's study was used to compare with simulated data [59]. In Ma's study, indoor moisture was tested experimentally. Since indoor humidity strongly influences DPT, the accuracy of the simulated humidity distribution was verified by experimental conditions based on Ma's work. However, the experimental conditions in Ma's study were not related to pre-dehumidification, which is the focus of this study. A pre-dehumidification experiment was therefore conducted in an environmental chamber. The details of the two validations are given in the following subsection.

2.6.1. Verification of indoor humidity condition

The experimental study conducted by Ma et al. was first chosen to verify the accuracy of simulating the humidity distribution using CFD software [59]. The schematic diagram of the laboratory in Ma's study is shown in Fig. 5(a). Points 1 to 5 in the figure were used to predict the indoor humidity distribution in the validation study. Fig. 5(b) shows the comparisons of humidity ratios obtained from the experimental measurement and the simulation. It is evident that the simulated data were consistent with most of the experimentally measured data. Fig. 5(c) shows the differences between measured and simulated values. Point 1 exhibits a deviation and has a large difference in the initial stage; Ma et al. [59] mentioned that the fluctuation of the experimental measurement data was caused by the instability of the system in the initial stage. The difference between the experimental and simulation data may have been relatively large because Point 1 was close to the entrance. The simulations of points 2 to 5 were largely consistent with the experimental data.

2.6.2. Verification of the pre-dehumidification stage

The field test was carried out in an environmental chamber at Shandong Jianzhu University, China. The dimensions of the chamber were 5.65 m × 4.9 m × 2.19 m. An SV system was adopted in the environmental chamber, in which air was blown in from two air inlets 1.36 m above the floor and out of two air outlets in the ceiling. The sizes of air inlet and outlet were, respectively, 0.29 m × 0.19 m and 0.27 m × 0.17 m. The layout of field test points is shown in Fig. 6(a). There are eight measuring points to test indoor air temperature and humidity. The field test environment is shown in Fig. 6(b). The temperature of the floor in the environmental chamber was 23.75 °C, and the temperature of the surrounding walls ranged from 25 to 27 °C.

Before the pre-dehumidification experiment, the air inlets and outlets were closed, and two humidifiers and a radiator were used to heat and humidify the indoor environment to create a high-temperature and high-humidity environment. An electric fan was used to constantly distribute the air evenly. When the indoor temperature was maintained at 27–28 °C, the relative humidity was between 70 and 80%, and the air DPT was not higher than the floor surface temperature. Then the humidifiers, heater, and fan were turned off, and the SV system was opened for dehumidification. To determine the variation of air temperature and humidity at a section 0.1 m above the floor, five measuring points were arranged, each a distance of 0.1 m from the floor. Their positions are shown in Fig. 6(c). The average value at the five measuring points was compared with the simulated value. Other measuring points were arranged at distances of 0.6, 1.1, and

Table 5
Temperature and humidity differences for different grids.

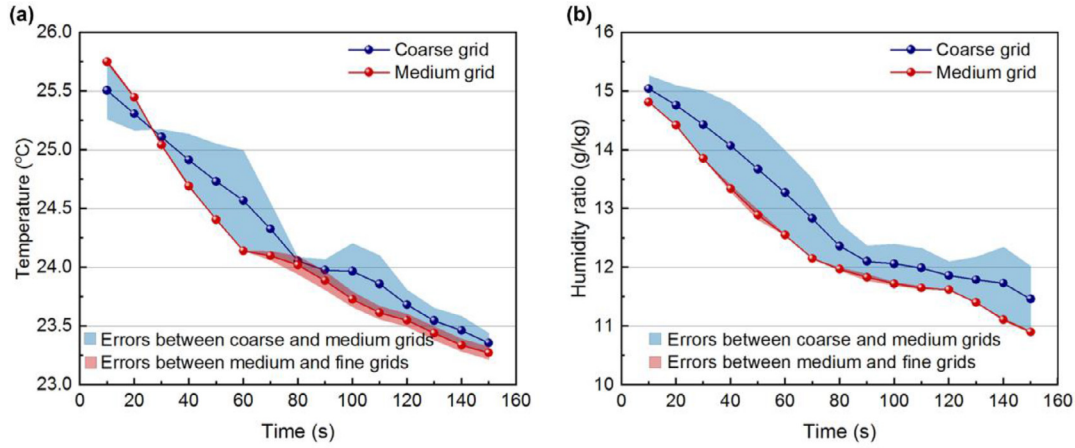| Item	Total number of elements	Temperature maximum difference (°C)	Humidity maximum difference (g/kg)
Coarse grid	337,542	–	–
Medium grid	529,276	0.084	0.198
Fine grid	836,336	0.058	0.093

Fig. 4. Grid independence analysis of numerical simulation. (a) Temperature vs, time at $z = 0.1$ m. (b) Humidity ratio vs. time at $z = 0.1$ m.
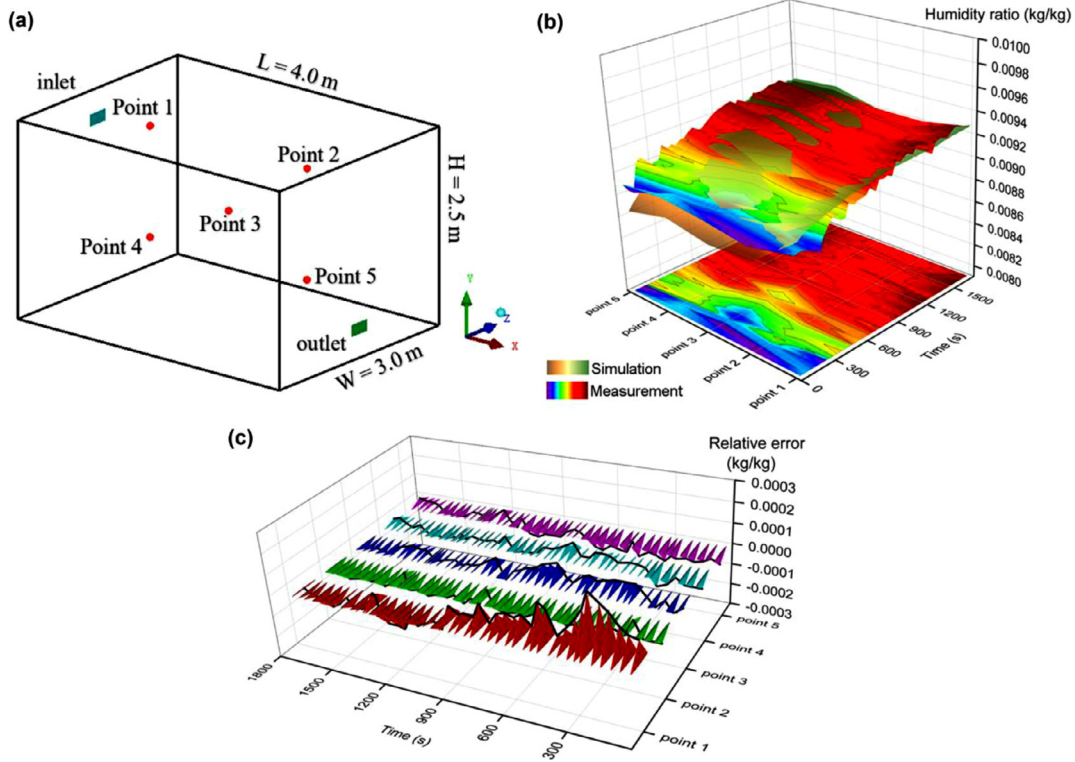

Fig. 5. Validating the results of the established CFD model. (a) Locations of measuring points [59]. (b) Comparison of measured and simulated values of the humidity ratio. (c) Differences between measured and simulated values.

1.8 m above the floor to observe the variation of temperature and humidity in the vertical direction. The specific locations are shown in Fig. 6(d).

2.6.3. Verification of pre-dehumidification stage

Two dehumidification tests were carried out in the environment chamber with different values of V_{as}. The boundary and initial conditions are given in Table 6. Fig. 7 shows the comparative results of the experiment and the simulation. Figs. 7(a) and (c) are the comparisons of DPT at section $z = 0.1$ m for $V_{as} = 0.018$ and 0.015 m³/s, respectively. It can be seen from the figures that the experiment and simulation are quite consistent, with maximum differences of 0.23 and 0.24 °C, respectively. Since it is difficult to control the temperature and humidity to have the same values in different experimental tests, the dehumidification times for DPT to drop by 1 °C were compared.

Table 6
The setting-up parameters of dehumidification tests.

Item	Experiment 1	Experiment 2	Unit
V_{as}	0.018	0.015	m³/s
T_{ini}	27.84	28.3	°C
H_{ini}	71.96	73.61	%
DPT	22.38	23.19	°C
T_{as}	21.2		°C
H_{as}	41.93		%

As shown in Fig. 7(a), when $V_{as} = 0.018$ m³/s, the DPT decreased by 1 °C, which took 62 s in the experiment and 64 s in the simulation. Fig. 7(c) shows that when $V_{as} = 0.015$ m³/s, the DPT decreased by 1 °C, which took 66 s in the experiment and 70 s in the simulation. The ex-

JID: ENBENV [m5GeSdc;September 7, 2022;18:55]

ARTICLE IN PRESS

M. Su, J. Liu, M.K. Kim et al. Energy and Built Environment xxx (xxxx) xxx
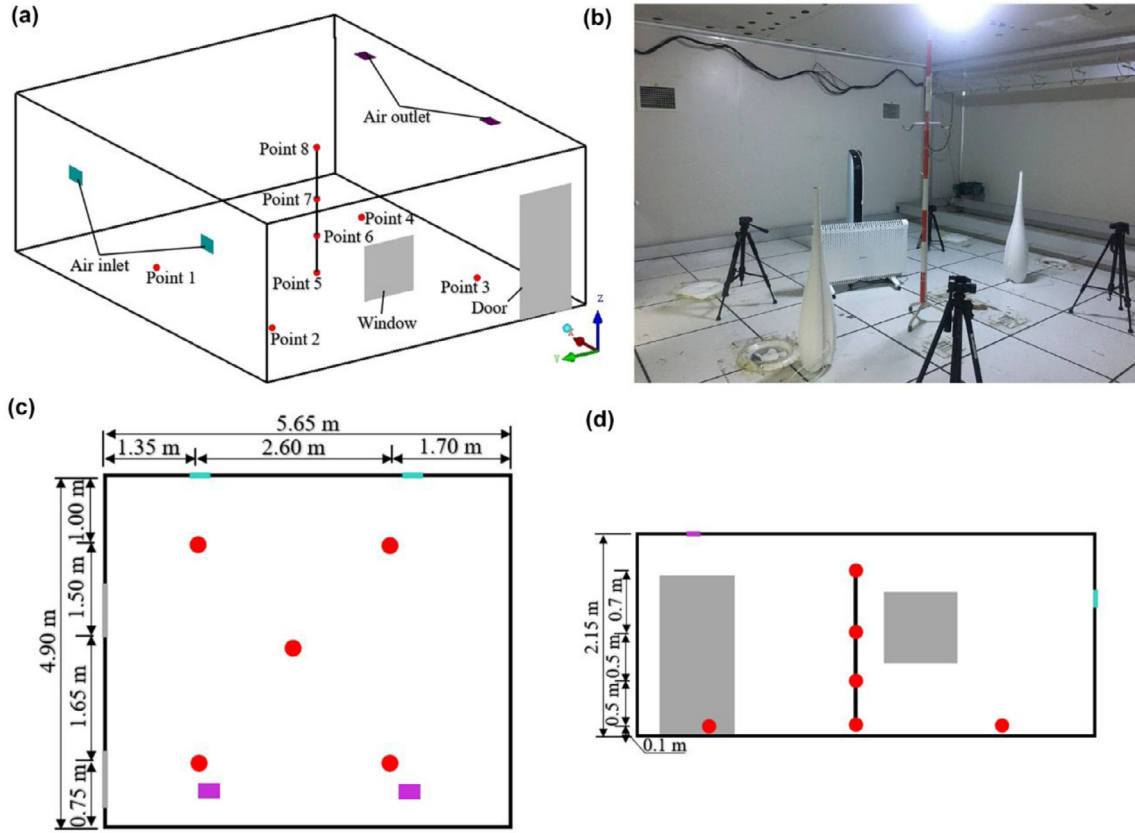

Fig. 6. The arrangement of measuring points for pre-dehumidification experiment. (a) 3D view of the experimental environment chamber. (b) Field-test environment in the environment chamber. (c) Top view of the measuring points. (d) Side view of the measuring points.

periment showed that increasing V_{as} can shorten the dehumidification time. Figs. 7(b) and (d) show the comparison of temperature at 0.6, 1.1, and 1.8 m away from the floor for V_{as} = 0.018 and 0.015 m^3/s. It can be seen from the figures that the measured and simulated data are quite consistent. As shown in Fig. 7(b), when V_{as} = 0.018 m^3/s, the maximum differences at 0.6, 1.1, and 1.8 m were, respectively, 0.17, 0.12, and 0.08 °C. As shown in Fig. 7(d), when V_{as} = 0.015 m^3/s, the maximum differences at 0.6, 1.1, and 1.8 m were, respectively, 0.29, 0.24, and 0.21 °C. This satisfactory consistency indicates that the accuracy of this model is sufficient for further study following the above verification.

2.7. BP neural network optimized by genetic algorithm

2.7.1. BP neural network

In recent years, ANN procedures have shown excellent performance in various prediction applications [60,61]. Their ability to learn new data and their adaptive performance make them ideal choices in many applications [48]. A BP neural network is a kind of multi-layer feedforward neural network, which adopts the error back propagation learning algorithm. Its basic idea is the gradient descent method, which uses gradient search technology to minimize the mean square difference of the actual output value and the expected output value of the network. The BP algorithm includes two processes: signal forward propagation and error back propagation. The error output is calculated in the direction from input to output, while the adjustment weight and threshold are calculated in the direction from output to input.

Stochastic gradient descent has been used as the optimizer to adjust weights and bias values, which helps to reduce the error rate between the predicted and the target output [62]. After signal forward propagation and error back propagation, the adjustment of weight and thresh-

old value is repeated until reaching the pre-set number of learning and training, or the output error is reduced to an allowable degree [63]. Therefore, the BP neural network was adopted in this study. Five input parameters and two output parameters are selected to define the numerical results of the neural network system. The initial setting of weight and bias are important for training of the BP neural network. According to Liu's study [64], the weights and biases are randomly initialized within the range of [−1, 1] in this study. The input parameters are V_m, T_{as}, H_{as}, V_{as}, T_{floor}; the output parameters are τ_{pre} and E_{pre}; and the number of neurons in the hidden layers is set to be 10. The structure of the neural network is shown in Fig. 8.

The transfer function used in this study was the tangent sigmoid function, and root mean square error (RMSE) was used as the evaluation index of model accuracy, which can be expressed by Eq. (4) below. Furthermore, the coefficient of determination (R^2), which is a measure of the degree of linear correlation between two study variables, can be expressed by Eq. (5) below. The simulated data were divided into two parts, 80% of which were randomly selected for BP neural network training and 20% for verification.

$$RMSE = \sqrt{\frac{1}{n} \sum_i |\hat{o}_i - o_i|^2} \tag{4}$$

$$R^2 = 1 - \frac{\sum_{i=0}^{n} (\hat{o}_i - \bar{o}_i)^2}{\sum_{i=0}^{n} (o_i - \bar{o}_i)^2} \tag{5}$$

where n is the number of data sets, $\hat{o}_i$ is the predicted value, and o_i is the simulated value.

2.7.2. Genetic algorithm

Although the traditional BP neural network has been widely used, it has many defects, including slow learning convergence speed, the fact
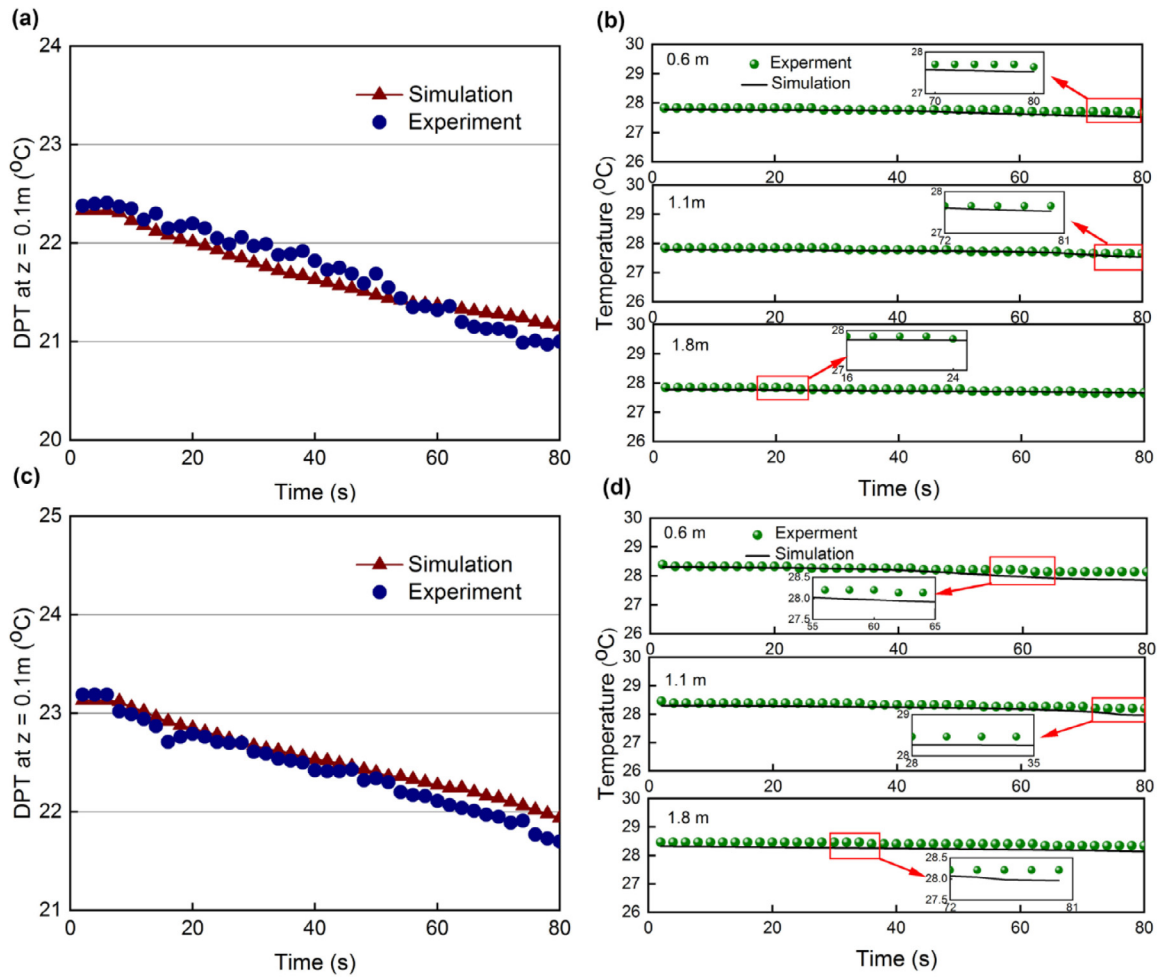
Fig. 7. Comparisons of experiment and simulation. (a) Variation of DPT at section $z = 0.1$ m when $V_{as} = 0.018$ m^3/s. (b) Variation of temperature in the vertical direction when $V_{as} = 0.018$ m^3/s. (c) Variation of DPT at section $z = 0.1$ m when $V_{as} = 0.015$ m^3/s. (d) Variation of temperature in the vertical direction when $V_{as} = 0.015$ m^3/s.
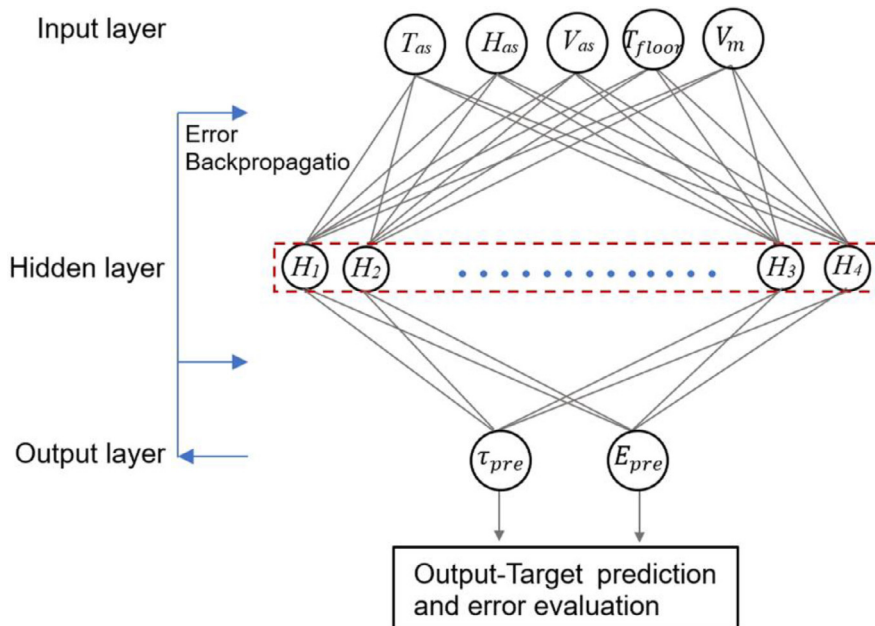
Fig. 8. Structure of BP neural network.

ARTICLE IN PRESS

JID: ENBENV　　　　　　　　　　　　　　　　　　　　　　　　　　　　　[m5GeSdc;September 7, 2022;18:55]

M. Su, J. Liu, M.K. Kim et al.　　　　　　　　　　　　　　　　　　　Energy and Built Environment xxx (xxxx) xxx

Crossover

A: 1100 0101 1111 ➡ A: 1100 0101 *0000*
B: *1111 0101 0000* ➡ B: *1111 0101* 1111

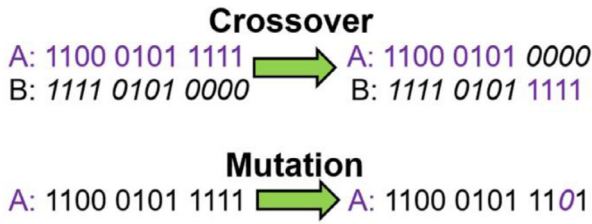**Mutation**

A: 1100 0101 1111 ➡ A: 1100 0101 11*0*1

Fig. 9. The crossover and mutation processes in GA [69].

that convergence to a global minimum cannot be guaranteed, and that the network structure is not easy to determine [51]. Therefore, the BP neural network needs to be improved.

Most BP neural networks use a gradient descent method. The advantage of this method is that it has only one direction and is fast in local optimization, but it easily falls into a local minimum, resulting in a low global optimization performance. GA, one of the gradient-free direct methods, has been successfully applied for optimization on HVAC system controls [65], green building design [66], and thermal and energy performances of refrigeration systems [67]. GA can search in multiple regions of solution space at the same time, and is able to jump from a local optimum and get the global optimum. GA is used to improve the weights and thresholds of BP neural network, and the convergence speed and accuracy of prediction model are improved [51].

Therefore, based on the defect analysis of the BP neural network, GA is used to improve the accuracy of BP neural network in this study. Its working principle comes from reproduction and natural selection in biological processes. The algorithm has high computing speed, can calculate and constrain any form of objective function, and can also accelerate the convergence speed of the BP neural network and improve its generalization ability and learning ability. GA is made up of five steps:

coding, fitness calculation, operator selection, exchange operation, and mutation operation [68].

On the basis of individual gene expression, the phenomena of crossover and mutation in the process of heredity are simulated by genetic operators, and the population is selected by generation, so as to obtain an optimal individual. GA composed of 12 bits is presented in Fig. 9 to explain the process of crossover and mutation.

2.7.3. Establishment of prediction model of GA-BP

GA optimization of a BP neural network is divided into three parts: First, the structure of the BP neural network is determined according to the number of input and output parameters of the fitting function, and the length of the GA is determined. Second, the weights and thresholds of a BP neural network are optimized by GA. Each individual in the population contains a network ownership value and threshold. The individuals calculate the individual fitness value through a fitness function, and GA through selection, crossover, and mutation operations to find the optimal fitness value corresponding to the individual [63]. Third, BP neural network prediction. The optimal individual obtained by GA is used to assign the initial weight and threshold value of the BP neural network. The BP neural network is then used for local optimization, and the predicted value of the BP neural network with global optimal solution is obtained. Its algorithm flowchart is shown in Fig. 10. The implementation steps are as follows.

First, the individual real numbers are encoded. Under the condition that the network structure is known, it can form a neural network whose structure, weight, and threshold are determined. With the prediction error between the output and the expected output of the absolute value and E as fitness of F, the calculation formula is as follows [63].

$$F = k \left(\sum_i^n abs(y_i - o_i) \right) \tag{6}$$
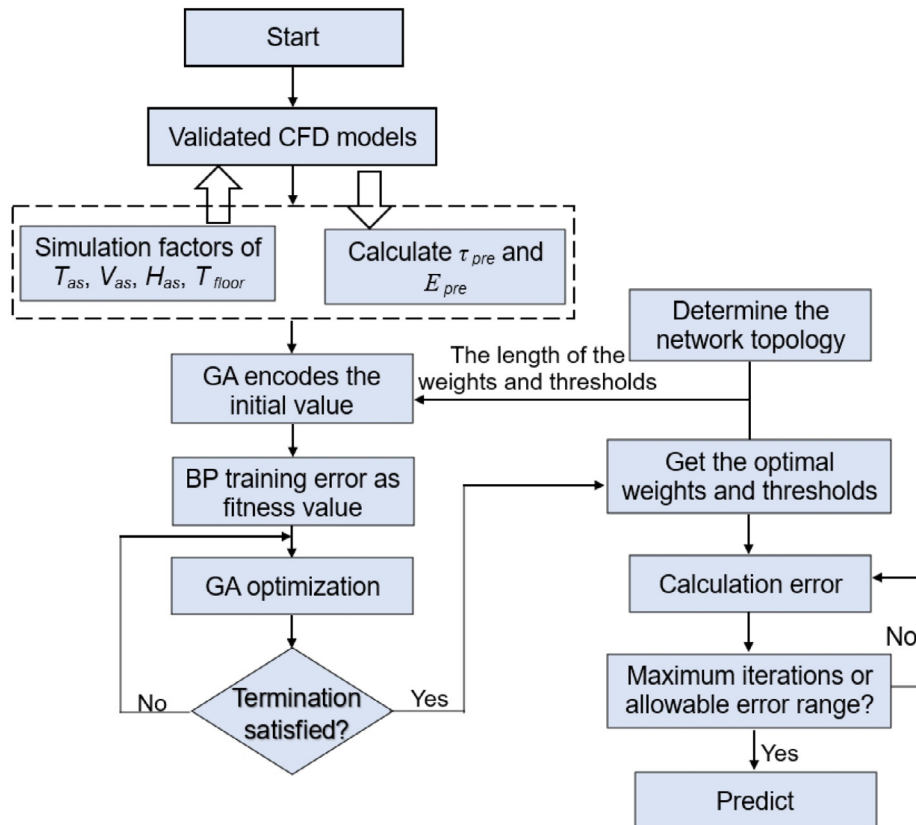
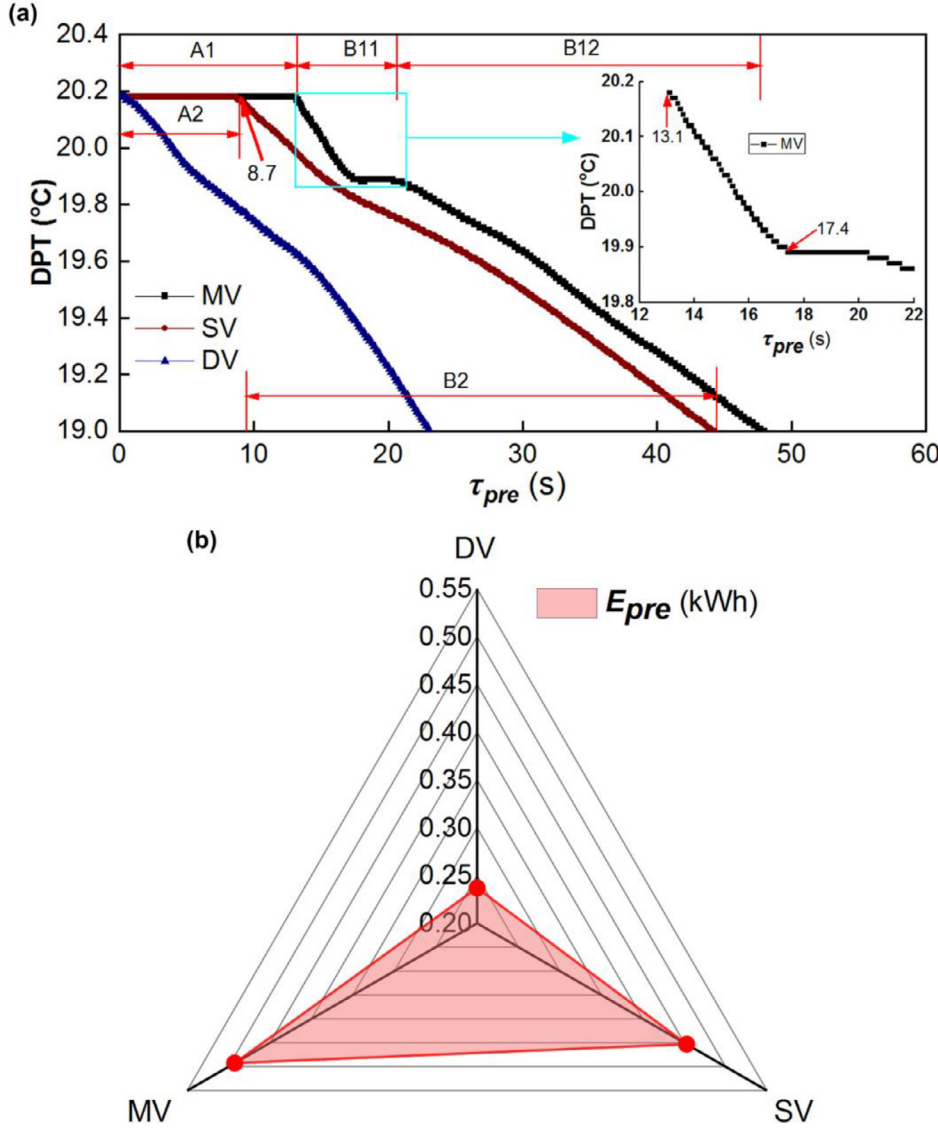**Fig. 10.** The framework of the BP neural network optimized by GA.

Fig. 11. Comparison of different ventilation systems. (a) Variation of DPT at $z = 0.1$ m. (b) Variation of E_{pre}.

where n is the output node number of the network, y_i is the expected output of the ith node of the BP neural network, o_i is the predicted output of the ith node, and k is a coefficient.

The work reported here chooses the roulette method, and the selection probability P_i of each individual is, from

$$f_i = k/F_i,$$ (7)

found to be

$$P_i = \frac{f_i}{\sum_{j=1}^{N} f_i}$$ (8)

In Eq. (7), F_i is the fitness value of individual I and k is the coefficient. In Eq. (8), N is the number of individuals in the population.

The cross-operation method of the k chromosome a_k and the l chromosome a_i in the jth bit is

$$\left. \begin{array}{l} a_{kj} = a_{kj}(1-b) + a_{lj}b \\ a_{lj} = a_{lj}(1-b) + a_{kj}b \end{array} \right\}$$ (9)

where b is a random number between 0 and 1.

When the jth gene a_{ij} of the ith individual is selected for mutation, the operation is as follows:

$$a_{ij} = \left\{ \begin{array}{l} a_{ij} + (a_{ij} - a_{max}) \times f(g), r > 0.5 \\ a_{ij} + (a_{min} - a_{ij}) \times f(g), r \leq 0.5 \end{array} \right\}$$ (10)

where a_{max} is the upper bound of gene a_{ij}, a_{min} is the lower bound of gene a_{ij}, $f(g) = r_2(1 - g/G_{max})$, r_2 is a random number, g is the current iteration number, G_{max} is the maximum number of evolutions, and r is a random number between 0 and 1.

3. Results

3.1. CFD simulation results

3.1.1. Comparison of different ventilation systems

In Fig. 11 different ventilation systems are compared. Fig. 11(a) shows the variation of DPT with dehumidification time at $z = 0.1$ m for different ventilation systems. With other conditions the same, it can be seen that the longest τ_{pre} was 48 s in the MV system, and the shortest τ_{pre} was 23.1 s in the DV system. Compared with SV and MV systems, the DV system can, respectively, save 47.8% and 51.87% dehumidification time. For the SV system, the pre-dehumidification stage was divided into two stages: Stage A2 (0–8.7 s) DPT was kept
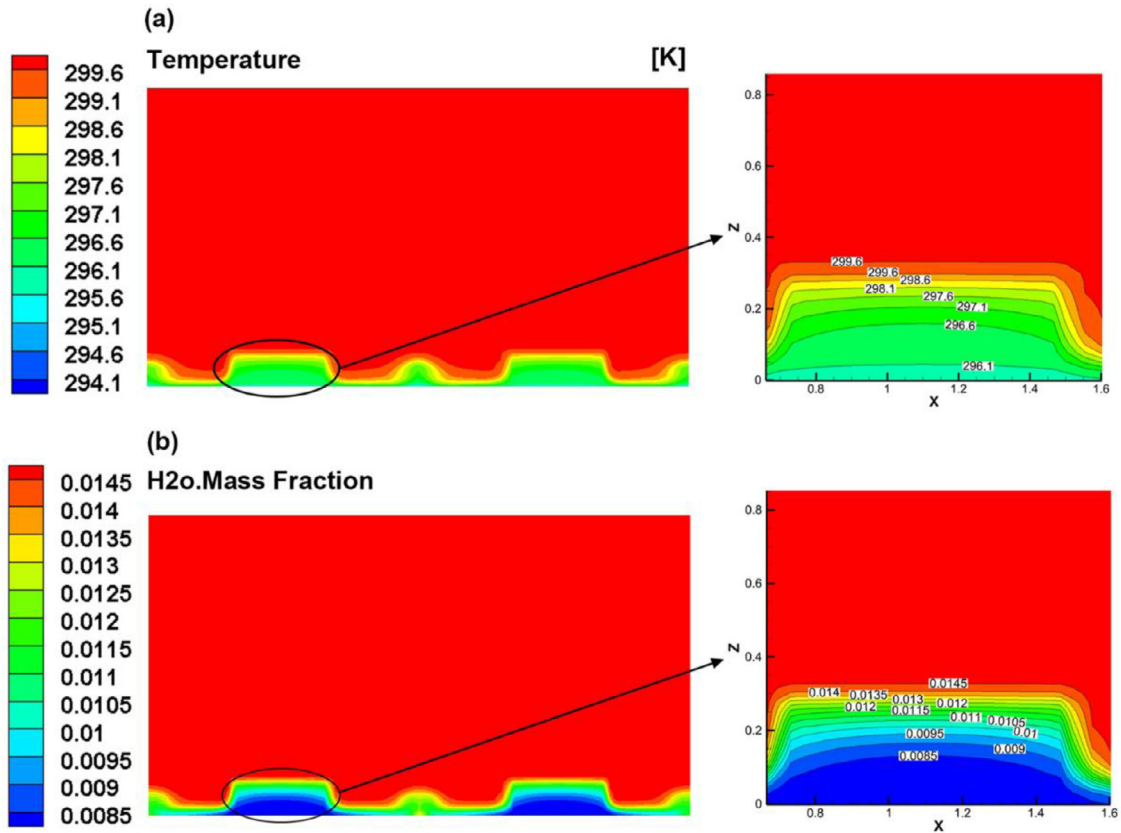
Fig. 12. The air contours at $y = 0.1$ m at $\tau = 5$ s in the DV system. (a) Air temperature contour. (b) Air humidity contour.

constant and the central space was dehumidified. In Stage B2 (beginning after 8.7 s), with the dehumidification of the space, the DPT decreased. For the MV system, the pre-dehumidification stage can also be divided into two stages. Stage A1 (0–13.1 s) DPT was kept constant and the upper space was dehumidified; in Stage B1 (beginning after 13.1 s), with the dehumidification of the space, the DPT decreased. Stage B1 of MV can be divided further into Stage B11 (13.1–17.4 s), which DPT decreased sharply with the dehumidification in space, and Stage B12 (beginning after 17.4 s), which DPT decreased slowly with the dehumidification in space, presenting a stepped shape.

This behavior occurs because the locations of the air supply inlets of the three ventilation systems are different. The shortest distance between inlet and floor was 0.1 m, for DV. The SV distance was 1.15 m, and the greatest distance was 2.2 m, for MV. This study focused on the variation between the DPT of air near the floor and the floor temperature. In SV and MV systems, fresh air was delivered through higher air inlets, and it took a certain amount of time for the air to settle to the floor. Therefore, the DPT in these two ventilation modes experiences a constant stage, which will be analyzed in detail in section 4.1.2. Fig. 11(b) shows the comparison of E_{pre} for different ventilation systems. In MV, SV, and DV systems, the values of E_{pre} were, respectively, 0.493, 0.453, and 0.237 kWh. E_{pre} was 8.05% less in the SV system than in the MV system, and 43.8% less in the DV system than in the MV system. Therefore, in comparing the energy-saving effect of pre-dehumidification, DV provided the greatest energy saving, mainly due to the strong influence of τ_{pre} on energy consumption. The longer is τ_{pre}, the greater is E_{pre}.

3.1.2. Distributions of the indoor air temperature and humidity

In order to further and more clearly explore the variation of indoor air temperature and humidity in the pre-dehumidification stage in the three ventilation systems, the section $y = 0.1$ m was selected for studying

the temperature and humidity environment. Fig. 12 exhibits the variation of temperature and humidity at section $y = 0.1$ m in the DV system at $\tau = 5$ s. As can be seen from the figure, in the DV system, where the air supply inlet is closer to the floor, the temperature and humidity at the bottom of the room were usually lower, while the temperature and humidity gradually increased from bottom to top. Figs. 13(a) and (b) exhibit the variation of temperature and humidity at section $y = 0.1$ m in the SV and MV systems, respectively. Compared with the DV system, the low-temperature and low- humidity air transported by the SV and MV systems obviously doesn't reach the floor as quickly when fresh air enters the room.

The temperature contour line of 297.15 K (24 °C) and humidity contour line of 0.01 were taken as an example. In the DV system, this temperature contour line was 0.2 m above the floor, and the 0.01 contour line was also located at this same height. In the SV system, the 297.15 K (24 °C) temperature contour line and also the 0.01 humidity contour line was 1.2 m above the floor. In the MV system, the two contour lines were also at the same height above the floor, 1.9 m. This explains why there is a phase in which the DPT remains constant in the SV and MV systems.

Fig. 14(a) shows the variation of the temperature and humidity at section $y = 0.1$ m when the SV system was ventilated for 8.7 s. At this point, the low temperature and low humidity air had reached the floor after a period of settlement, and then, with an increase of ventilation time, the DPT of the air near the floor gradually decreased. Fig. 14(b) exhibits the variation of temperature and humidity at section $y = 0.1$ m when the MV system was ventilated for 13.1 s. It can be seen from this figure that the low-temperature and humid air reached near the floor, and that the DPT of the air near the floor gradually decreased. Since the air inlet of the MV system is higher than that of the SV system, the low temperature and humidity air from the MV system take a longer time to settle to the floor than for the SV system. This explains why the DV
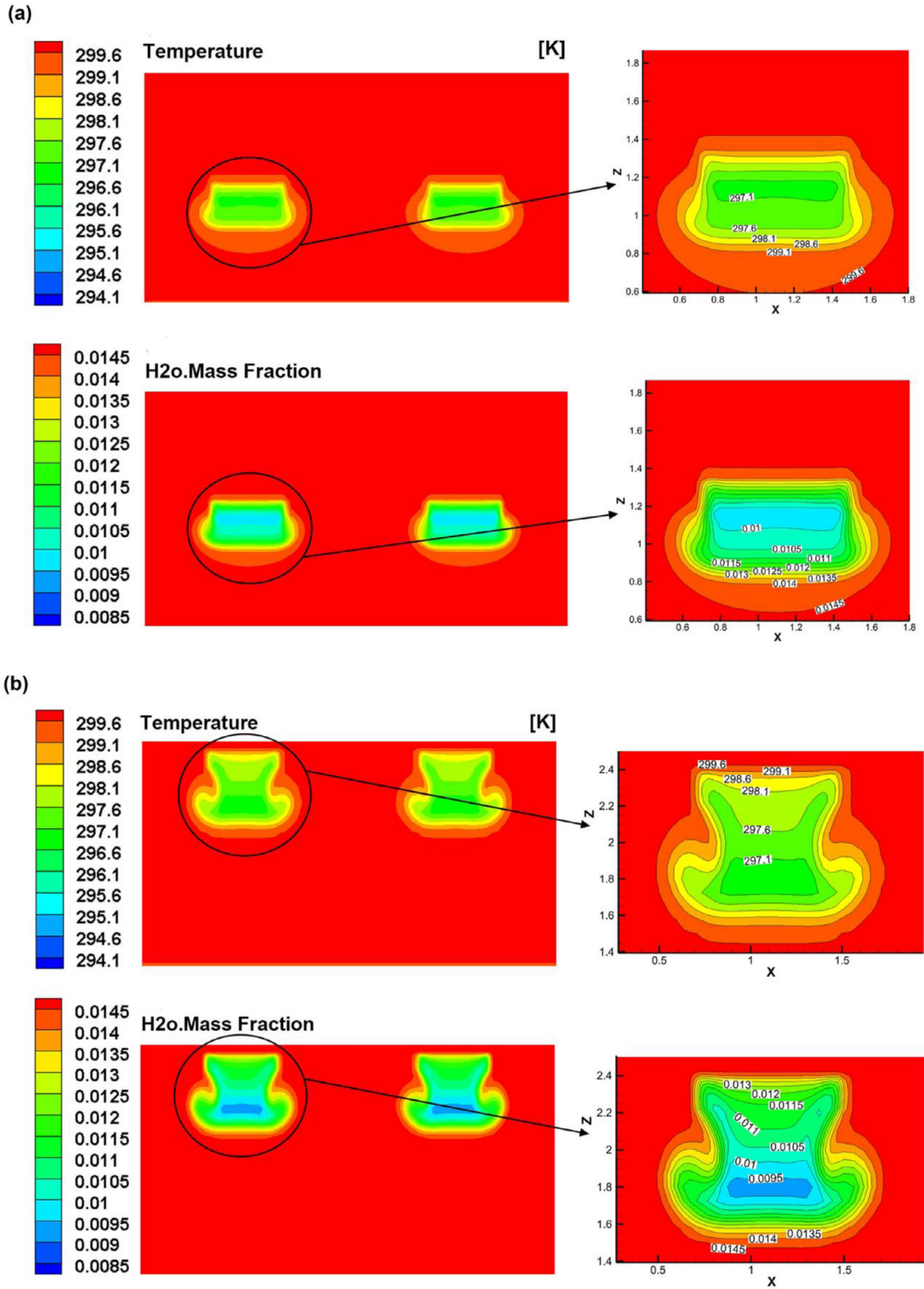
Fig. 13. Air temperature and humidity contours at $y = 0.1$ m at $\tau = 5$ s in (a) the SV system and (b) the MV system.
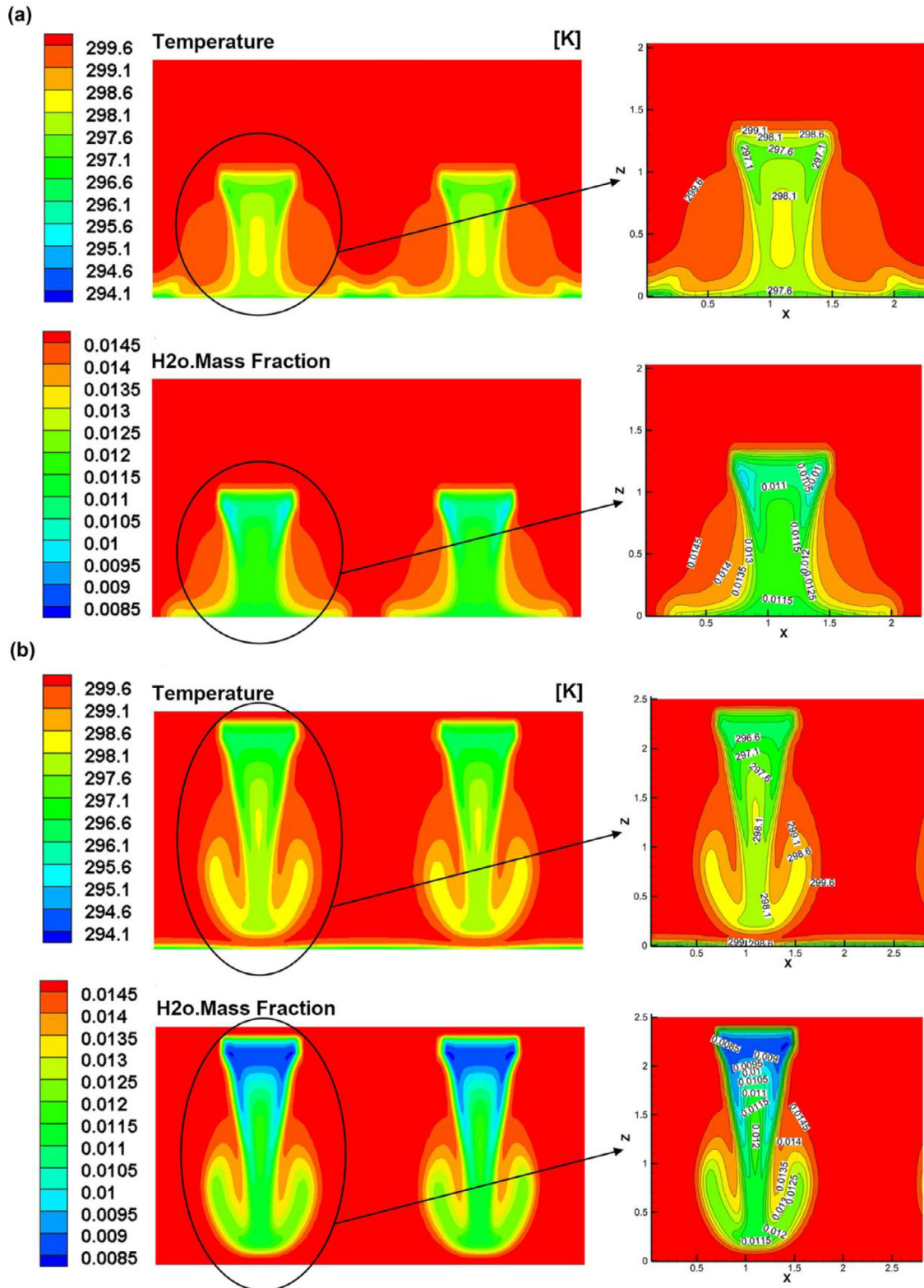
Fig. 14. Air temperature and humidity contours at $y = 0.1$ m in different ventilation systems. (a) At $\tau = 8.7$ s in the SV system. (b) At $\tau = 13.1$ s in the MV system.

system has the shortest τ_{pre}, followed by the SV system, and then by the MV system, which has the longest τ_{pre}.

3.2. Verification of the established prediction model

80% of the data were randomly selected for neural network training, and the remaining data were used for validation. The number of iter-ations of the neural network was 1000, the learning rate was 0.1, and the expected error was 0.00001. The parameters of the GA were set as follows: population size, 20; number of genetic iterations, 50; crossover probability, 0.7; and mutation probability, 0.01. When the loss function curve decreases to a certain value, and remains stable with an increase of the number of iterations, the training is considered to have achieved convergence [70]. Fig. 15 shows the fitness curve of the GA. The
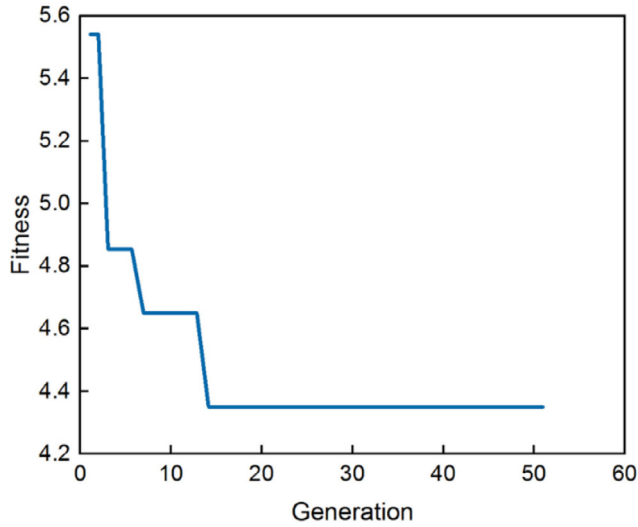
ARTICLE IN PRESS

JID: ENBENV   [m5GeSdc;September 7, 2022;18:55]

M. Su, J. Liu, M.K. Kim et al.   Energy and Built Environment xxx (xxxx) xxx

Fig. 15. Variation of fitness with the number of genetic iterations.

Table 7
Comparison of predicted results for BP and GA-BP models.

	τ_{pre}		E_{pre}	
	BP	GA-BP	BP	GA-BP
RMSE	5.618	1.994	0.051	0.042
R^2	0.913	0.973	0.935	0.956

Fig. 16(a) exhibits a comparison between the predicted results of the GA-BP model and the BP model for τ_{pre} with the original simulated data. It can be seen qualitatively that the prediction effect of the GA-BP model is significantly better than that of the BP model, and the predicted value of the GA-BP neural network is basically consistent with the simulated value of CFD. Fig. 16(b) compares the differences between the predicted results of the GA-BP model and the BP model with the simulated original data of τ_{pre}. It can be seen that the maximum predicted difference was 3 s, less than the 14 s of the BP model. From Table 7 it can be concluded that the RMSE and R^2 of τ_{pre} predicted by the BP model were 5.618 and 0.913, respectively, while the RMSE and R^2 predicted by the GA-BP model were 1.944 and 0.973, respectively.

Fig. 16(c) compares the predicted results of the GA-BP and BP models for E_{pre} with the simulated original data. The predicted value of the GA-BP neural network has a high degree of fit with the simulated value of CFD. Fig. 16(d) compares the differences between the predicted re-

fitness does not decrease after the 14th genetic iteration—that is, the optimal fitness value was reached. Adjusting the network structure and selecting a reasonable learning rate were adopted in this study, which improves the generalization capability of the predicted model [71].
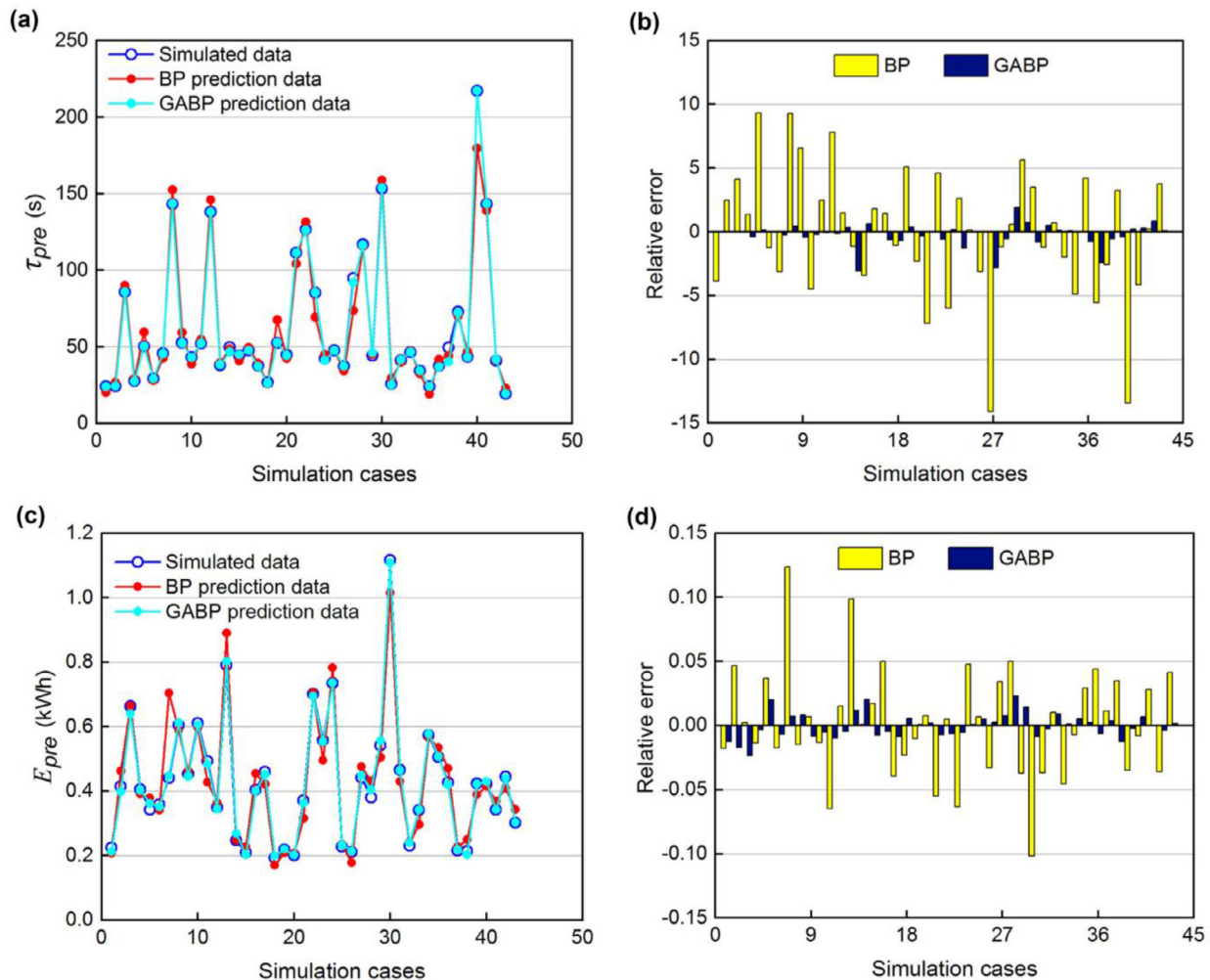

Fig. 16. Comparisons of the predicted and simulated values of (a) τ_{pre}, (b) the relative error of τ_{pre}, (c) E_{pre}, and (d) the relative error of E_{pre}.
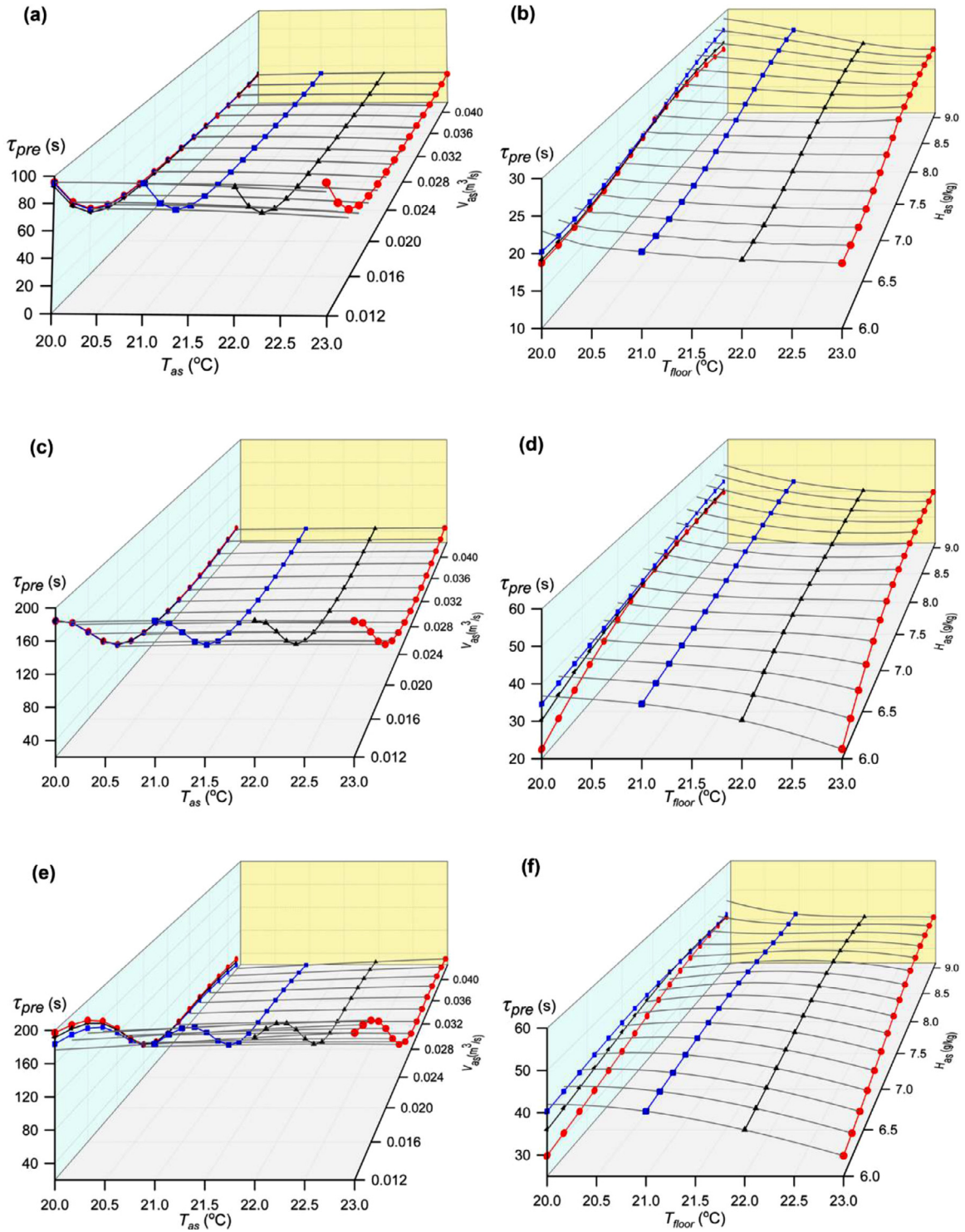
Fig. 17. Three-dimensional diagrams of variation trends of τ_{pre} for different influencing factors. (a) The effect of T_{as} and V_{as} in the DV system. (b) The effect of H_{as} and T_{floor} in the DV system. (c) The effect of T_{as} and V_{as} in the SV system. (d) The effect of H_{as} and T_{floor} in the SV system. (e) The effect of T_{as} and V_{as} in the MV system. (f) The effect of H_{as} and T_{floor} in the MV system.

sults of the GA-BP model and the BP model with the simulated original data of E_{pre}. It can be seen that the maximum predicted difference of the GA-BP model was 0.0248 kWh, less than the 0.125 kWh of the BP model. In Table 7 it can be seen that the RMSE and R^2 of E_{pre} predicted by the BP model were 0.051 and 0.935, respectively, while the RMSE and R^2 predicted by the GA-BP model were 0.042 and 0.956, respectively.

Based on the above analysis, it can be concluded that both the GA-BP and BP models can reflect relatively well the internal relationship between τ_{pre} and E_{pre} and input variables, but it is obvious that the prediction model optimized by GA-BP has higher prediction accuracy. Note that the computational times for training with GA-BP and BP were about 0.30 hour and 0.08 hour, respectively. Therefore, taking into account the accuracy of the perdition
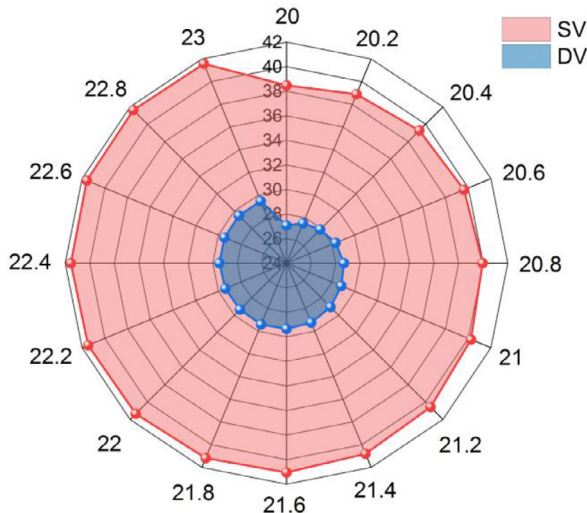
Fig. 18. Variation of τ_{pre} with T_{as} in the DV and SV systems.

Table 8
The data ranges for prediction.

Decision variable	Range	Unit
V_m	DV, SV, MV	N.A.
T_{as}	20–23	°C
H_{as}	6–9	g/kg
V_{as}	0.012–0.042	m³/s
T_{floor}	20–23	°C

model, the GA-BP neural network was used for accurate estimation of τ_{pre} and E_{pre} according to the operating parameters from indoor environments.

3.3. Predicted results of GA-BP

3.3.1. Pre-dehumidification time

To determine the laws that govern the effects of the control factors on τ_{pre} and E_{pre}, larger ranges of the data were set based on the scopes of different parameters, as exhibited in Table 8. The data set was substituted into the trained GA-BP neural network model for prediction, and the effect of different control parameters on τ_{pre} and E_{pre} were obtained, as discussed below.

Fig. 17 shows a three-dimensional diagram of the variation trends of τ_{pre} in the DV, SV, and MV systems. Figs. 17(a), 17(c), and 17(e) show the effect of T_{as} and V_{as} on τ_{pre}; the gray line represents the variation of T_{as}. It is obvious in Fig. 17(c) that with an increase of T_{as}, τ_{pre} increases gradually in the MV system. Nonetheless, the effect of T_{as} on τ_{pre} in the DV and SV systems cannot be seen clearly in Figs 17(a) and 17(b). Therefore, these data were transformed into a two-dimensional curve, as shown in Fig. 18. It can be seen from this figure that τ_{pre} increases with an increase of T_{as}. In the SV system, with an increase of T_{as} from 20 to 23 °C, τ_{pre} increases from 38.50 to 41.57 s, a variation of 7.38%. In the DV system, τ_{pre} increases from 27.13 to 29.27 s, a variation of 7.31%. In the MV system, τ_{pre} increases by 16%. In order to see clearly the effect of V_{as} on τ_{pre} in the three systems, the curves of the variation of τ_{pre} with V_{as} when T_{as} = 21, 22, and 23 °C are shown in Figs 17(a), 17(c), and 17(e). It can be seen that τ_{pre} gradually decreases with an increase of V_{as}. When T_{as} = 21 °C, with an increase of V_{as} from 0.012 to 0.042 m³/s, τ_{pre} decreases by 66.97%, 71.71%, and 84.98% in the DV, SV, and MV systems, respectively. It follows that increasing V_{as} can effectively shorten τ_{pre}.

Figs. 17(b), 17(d), and 17(f) show the effect of T_{floor} and H_{as} on τ_{pre}; the gray line traces the variation of T_{floor}. As shown in these figures,

when H_{as} = 9 g/kg, with an increase of T_{floor} from 20 to 23 °C, τ_{pre} decreases by 20.14, 20.08, and 11.72%, respectively, in the DV, SV and MV systems. In order to see clearly the effects of H_{as} on τ_{pre} in the three systems, the curves of the variation of τ_{pre} with H_{as} when T_{floor} = 21, 22, and 23 °C are shown in Figs 17(b), 17(d), and 17(f). The projected curve shows that with a decrease of H_{as}, τ_{pre} decreases. When T_{floor} = 23 °C, with a decrease of H_{as} from 9 to 6 g/kg, τ_{pre} decreases by 28.12, 40.82 and 41.48%, respectively, in the DV, SV, and MV systems.

The main reason for this phenomenon is that τ_{pre} is determined principally by the air humidity ratio between indoor air and air supply—that is, the dehumidification rate. A high dehumidification rate has a short τ_{pre}, and vice versa. With increases of T_{as} and H_{as}, the air supply humidity ratio increases, and the difference in the humidity ratio of indoor air and air supply is reduced. Furthermore, the dehumidification speed becomes less, and the effect of the humidity ratio on the air DPT becomes greater. Therefore, with an increase of T_{as} and H_{as}, the dehumidification time is lengthened. With an increase of V_{as}, the dehumidification speed increases, which allows the indoor DPT to be rapidly reduced to its target difference from the value of T_{floor}. Therefore, with an increase of V_{as}, τ_{pre} is decreased. With an increase of T_{floor}, the set initial indoor air DPT increases, which means that the indoor air humidity ratio increases, resulting in an increase in the humidity ratio difference between the air supply and the indoor air, as well as an increase of dehumidification rate. Therefore, with the increase of T_{floor}, τ_{pre} decreased.

3.3.2. Pre-dehumidification energy consumption

Figs. 19(a) and 19(b) provide three-dimensional diagrams of the variation trends of E_{pre} in the DV system. Fig. 19(a) shows the effect of T_{as} and V_{as} on E_{pre}; the pink projection represents the variation of T_{as}. As can be seen from the figure, E_{pre} gradually decreases with an increase of T_{as}. Taking the projection of V_{as} = 0.032 m³/s as an example, with an increase of T_{as} from 20 to 23 °C, E_{pre} decreases from 0.275 to 0.256 kWh, a change of 7.05%. The blue projection represents the variation of V_{as}. As V_{as} increases, E_{pre} shows a tendency to fluctuate. Fig. 19(b) shows the effect of H_{as} and T_{floor} on E_{pre}; the pink projection represents the variation of T_{floor}. As can be seen from the figure, E_{pre} gradually decreases with an increase of T_{floor}. Taking the projection of H_{as} = 6 g/kg as an example, with an increase of T_{floor} from 20 to 23 °C, E_{pre} decreases from 0.219 to 0.109 kWh, a change of 50.2%. The blue projection represents the variation of H_{as}. With a decrease of H_{as} from 9 to 6 g/kg, E_{pre} varies by 58.36%.

Figs. 19(c) to 19(f) present three-dimensional diagrams of the variation trends of E_{pre} in the SV and MV systems. We take V_{as} = 0.032 m³/s as an example for analysis. In the SV system, with an increase of T_{as} from 20 to 23 °C, E_{pre} decreases from 0.56 to 0.43 kWh, a change of 23.2%. In the MV system, E_{pre} decreases by 9.47%. As V_{as} increases, E_{pre} shows a fluctuating trend. This indicates that the effect of V_{as} on E_{pre} is not significant in this study. It can be seen from Figs. 19(d) and (F) that the effects of H_{as} and T_{floor} on E_{pre} in the SV and MV systems have the same trend as that in the DV system. With a decrease of H_{as} and an increase of T_{floor}, E_{pre} gradually decreases.

The HVAC issues for heat transfer and energy usage in office spaces have not been successfully addressed using CFD techniques. According to Eqs. (4)—(6), the main reasons for this are the following: With variation of T_{as} and H_{as}, E_{pre} is related to τ_{pre} and to the difference in the enthalpies of the air supply and outdoor air. The greater the value of T_{as}, the smaller is the difference in the enthalpies of the air supply and outdoor air. Hence, if T_{as} increases, the energy consumption will decrease. However, with a variation of H_{as}, the difference in the enthalpies of the air supply and outdoor air is small. Therefore, the decisive factor affecting E_{pre} was found to be τ_{pre}. The smaller the value of H_{as}, the shorter is τ_{pre}, and thus E_{pre} is also smaller. As V_{as} varies, E_{pre} depends mainly on τ_{pre} and V_{as}. With an increase of V_{as}, τ_{pre} decreases. The two factors do have some effect on E_{pre}. Thus, E_{pre}
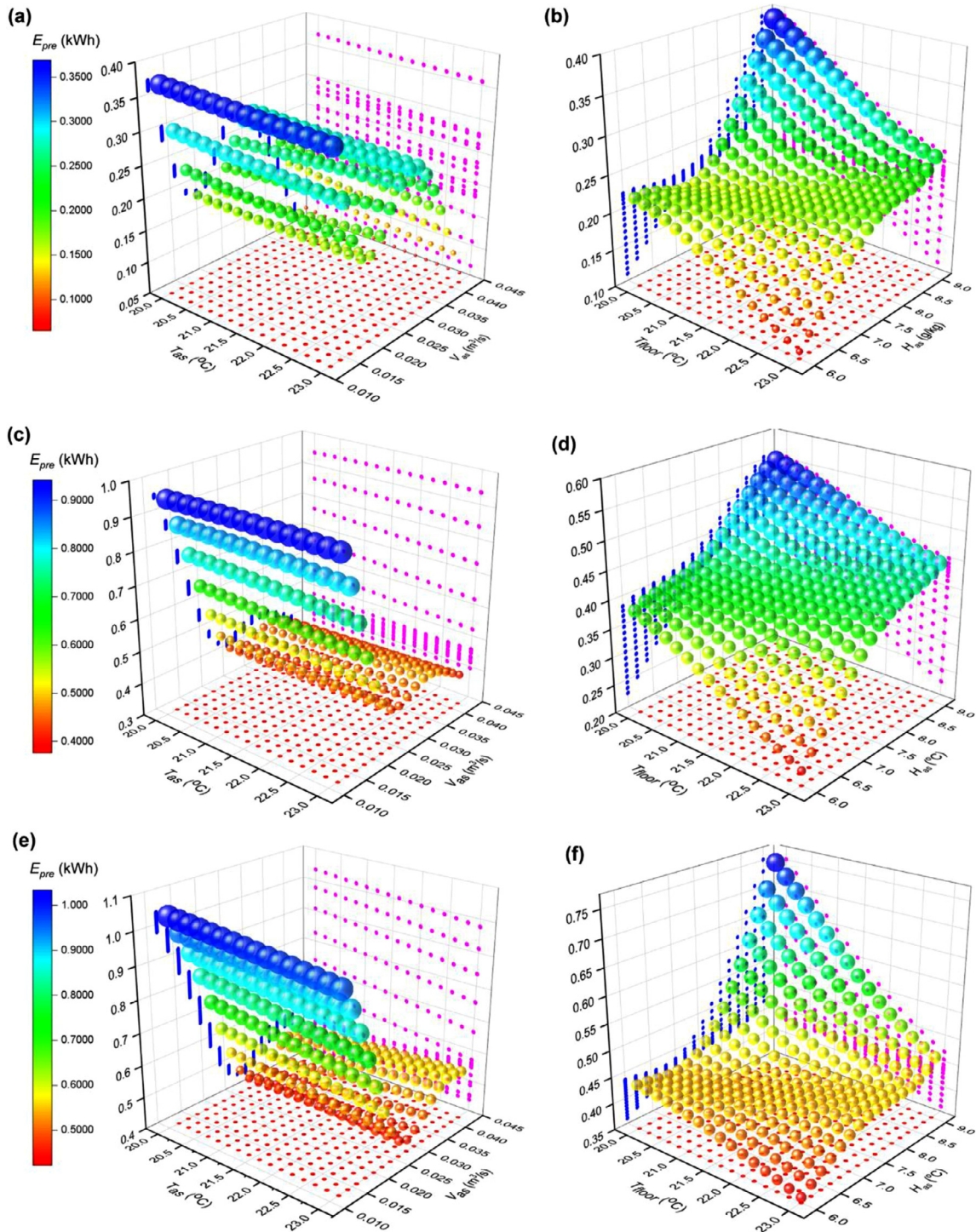
Fig. 19. Three-dimensional diagrams showing variation trends of E_{pre} with different influencing factors. (a) The effects of T_{as} and V_{as} in the DV system. (b) The effects of H_{as} and T_{floor} in the DV system. (c) The effects of T_{as} and V_{as} in the SV system. (d) The effect of H_{as} and T_{floor} in the SV system. (e) The effect of T_{as} and V_{as} in the MV system. (f) The effect of H_{as} and T_{floor} in the MV system.

fluctuates as V_{as} varies. With a variation of T_{floor}, E_{pre} depends only on τ_{pre}. With an increase of T_{floor}, τ_{pre} decreases, and E_{pre} gradually decreases.

4. Discussion

In view of the problem of moisture condensation in the application of an RFC system in office buildings, this work studied a venti-

lation system to be opened in advance for pre-dehumidification treatment before the space is occupied. The ANN approach is a generic technique for mapping the relationships between inputs and outputs without knowing the details of these relationships. Therefore, ANN was used to explore the effect of different factors on the pre-dehumidification time and energy consumption. The learning data were collected by CFD simulation, and then the trained neural network prediction model was used to replace CFD simulation and predict the time needed to

open the ventilation system in advance and the energy consumed in the pre-dehumidification stage. Compared with other similar studies, the unique advantage of this study is in its combination of CFD simulation and a neural network, which can predict the detailed situation of indoor air distribution. The effects of different factors on the pre-dehumidification stage in three ventilation systems were compared. Because of a shortcoming of the BP neural network—that its convergence is slow—if the problem is more complex, training time may be relatively long [51]. GA was used to optimize the BP neural network, so as to improve the accuracy of the prediction model. Finally, the GA-BP neural network prediction model can quickly predict the duration and energy consumption of pre-dehumidification for different initial conditions.

This study provides a novel and effective evaluation method for RFC pre-dehumidification control, but it has some limitations. Only five factors were considered that influence τ_{pre} and E_{pre}. The issues considered here have not yet been comprehensively considered, nor is the fitness of the model broad enough. Subsequent studies will consider more comprehensive factors. Although this study proved that ANN can effectively solve the problem of condensation of the floor surface in an RFC system, the resulting static model can only reflect the steady-state behavior of the pre-dehumidification process. However, the development of predictive control strategy needs to combine dynamic systems, so as to dynamically adapt to the constant adjustment of disturbance variation. Therefore, the dynamic neural network model is very important for understanding the complex relationship between inputs and outputs under transient conditions [72], which will be further studied.

In this study, the floor was assumed to be a constant-temperature surface. In radiant floor systems, the distribution of the floor surface temperature is an important parameter. The relationship between floor surface temperature and air DPT near the floor is a crucial factor in the prevention of condensation on a floor surface. Therefore, it is necessary to further analyze the influence of floor-surface temperature distribution on floor performance [73,74]. Furthermore, previous studies have shown that RFC systems are thermally inert, and that the floor temperature varies due to variations in the water supply temperature and flow rate. Therefore, it is necessary to analyze the dynamic thermal characteristics of radiant structures to more accurately predict the risk of floor condensation [75,76].

There is also a technical limitation in this work. We used 243 sample data points of neural network training obtained through simulation, which is relatively small. Therefore, the generalization ability of the prediction model is not high. Although this study considers adjusting network structure and learning rate to improve generalization ability, the methods are not comprehensive enough. In future study, more methods will be considered, including increasing the size of each batch to make the predicted model see more data in each iteration and prevent overfitting, adjusting the data distribution, doing the class of the training data set and selecting a reasonable training time to avoid overtraining [77].

The selection of air supply parameters was not considered comprehensively. The setting was based only on previous studies [54–56], without considering the performance of cooling coils. Although the air supply mode was considered as a variable in this study, the air supply parameters (e.g., air supply temperature) of air supply modes have specific input ranges [37]. Future studies will seek to comprehensively optimize the design of air supply parameters. Even though CFD simulation has great advantages in solving indoor problems, it puts a substantial demand on computing resources. Since CFD simulation takes a long time, it requires strict requirements on computer equipment to obtain more training data. CFD data dimension reduction is very important for improving the efficiency of database construction, training, and storage. In a certain accuracy loss range, the calculation and prediction speed can be realized quickly, thus reducing the calculation load and shortening the calculation time [78]. Therefore, more time will be devoted to computing in the future to achieve more rapid CFD simulation.

5. Conclusions

In this study, we developed predictive control strategies based on neural networks. Taking an office as the study object, a CFD simulation was carried out, and the accuracy of the model was verified by experiment. A BP neural network was proposed and optimized with the GA algorithm to predict the pre-dehumidification time (τ_{pre}) and pre-dehumidification energy consumption (E_{pre}) in an office room. The following conclusions are drawn.

The GA-BP neural network was more accurate and stable than the BP neural network. The R^2 values of τ_{pre} and E_{pre} were very high, reaching 0.9732 and 0.9557, respectively. The RMSE of τ_{pre} and E_{pre} were 1.994 and 0.0418, respectively. Therefore, the GA-BP neural network model established in this study can replace a CFD simulation to predict τ_{pre} and E_{pre}.

Under the same conditions, τ_{pre} in the DV system (with the lowest air inlet) was the shortest and in the MV system (with the highest inlet) was the longest. Relative to SV and MV systems, the DV system can save, respectively, 47.9% and 51.8% in τ_{pre}. In addition, due to the influence of the location of the air inlet, the pre-dehumidification stage can be divided into two stages in the SV and MV systems: a stage where the air DPT remains constant and a stage where the air DPT drops. Meanwhile, according to Eqs. (4)—(6), E_{pre} is affected mainly by τ_{pre}. In DV systems, τ_{pre} was the smallest and can save about 40% in energy consumption compared with MV systems, which have the largest τ_{pre}. Therefore, the combination of a DV system and an RFC system can achieve the best pre-dehumidification effect.

The prediction results of the GA-BP model show that for all three ventilation systems, V_{as} has the most obvious effect on τ_{pre}. In the MV system, it can save about 80% of τ_{pre}. V_{as} has the least effect on E_{pre}, which fluctuates as V_{as} is varied. The research reported in this paper can help building management departments design and select the most effective control strategy to operate an RFC system, and provide theoretical reference value.

Conflicts of interest

The authors declare that there is no conflicts of interest.

CRediT authorship contribution statement

Meng Su: Software, Data curation, Methodology, Writing – original draft, Formal analysis, Visualization. **Jiying Liu:** Conceptualization, Methodology, Supervision, Writing – review & editing, Project administration, Funding acquisition. **Moon Keun Kim:** Writing – review & editing, Formal analysis. **Xiaozhou Wu:** Writing – review & editing, Visualization.

Acknowledgments

References

[1] S. Zhan, A. Chong, Building occupancy and energy consumption: case studies across building types, Energy Built Environ. 2 (2) (2020) 167–174.

[2] Z. Jiao, J. Yuan, C. Farnham, et al., Deviation of design air-conditioning load based on weather database of reference weather year and actual weather year, Energy Built Environ. 1 (4) (2020) 417–422.

[3] Y. Li, L. Yang, B. He, et al., Green building in China: needs great promotion, Sustain. Cities Soc. 11 (2014) 1–6.

[4] Y. Tan, J. Peng, C. Curcija, et al., Study on the impact of window shades' physical characteristics and opening modes on air conditioning energy consumption in China, Energy Built Environ. 1 (2020) 254–261.

[5] K.N. Rhee, K.W. Kim, A 50 year review of basic and applied research in radiant heating and cooling systems for the built environment, Build. Environ. 91 (2015) 166–190.

[6] S. Minetto, S. Marinetti, P. Saglia, et al., Non-technological barriers to the diffusion of energy-efficient HVAC&R solutions in the food retail sector, Int. J. Refrig. 86 (2018) 422–434.

[7] P. Srivastava, Y. Khan, M. Bhandari, et al., Calibrated simulation analysis for integration of evaporative cooling and radiant cooling system for different Indian climatic zones, J. Build. Eng. 19 (2018) 561–572.

[8] J. Liu, M.K. Kim, J. Srebric, Numerical analysis of cooling potential and indoor thermal comfort with a novel hybrid radiant cooling system in hot and humid climates, Indoor Built Environ. 31 (4) (2022) 929–943.

[9] B. Yang, X. Ding, F. Wang, et al., A review of intensified conditioning of personal micro-environments: moving closer to the human body, Energy Built Environ. 2 (2021) 260–270.

[10] K. Dharmasastha, D.G.L. Samuel, S.M.S. Nagendra, et al., Impact of indoor heat load and natural ventilation on thermal comfort of radiant cooling system: an experimental study, Energy Built Environ. (2022) In press, doi:10.1016/j.enbenv.2022.04.003.

[11] V.R. Khare, R. Garg, J. Mathur, et al., Thermal comfort analysis of personalized conditioning system and performance assessment with different radiant cooling systems, Energy Built Environ. (2021) In press, doi:10.1016/j.enbenv.2021.09.001.

[12] GA 30329ASHRAE Handbook—HVAC Systems and Equipment, ASHRAE, Atlanta, 2016.

[13] S.A. MUMMA, Dedicated outdoor air in parallel with chilled ceiling system, Eng. Syst. 18 (11) (2001) 56–61.

[14] J. Niu, J. Burnett, Integrating radiant/operative temperature controls into building energy simulations, ASHRAE Trans. 104 (2) (1998) 210–217.

[15] Y. Yuan, X. Zhang, X. Zhou, A study on inherent correlation of thermal performances and condensation free control of the radiant system, Energy Build. 129 (2016) 19–31.

[16] H. Tang, X.-H. Liu, Y. Jiang, Theoretical and experimental study of condensation rates on radiant cooling surfaces in humid air, Build. Environ. 97 (15) (2016) 1–10.

[17] X. Zhu, J. Liu, X. Zhu, et al., Experimental study on operating characteristic for a combined radiant floor and fan coil cooling system in a high humidity environment, Buildings 12 (4) (2022) 499.

[18] J. Liu, X. Zhu, M.K. Kim, et al., A transient two-dimensional CFD evaluation of indoor thermal comfort with an intermittently-operated radiant floor heating system in an office building, Int. J. Archit. Eng. Technol. 7 (2020) 62–87.

[19] K.-N. Rhee, B.W. Olesen, K.W. Kim, Ten questions about radiant heating and cooling systems, Build. Environ. 112 (2017) 367–381.

[20] S.A. Mumma, Condensation Issues with Radiant Cooling Panels, IAQ Applications/Fall 2 (2001) 16–18.

[21] M. Amini, R. Maddahian, S. Saemi, Numerical investigation of a new method to control the condensation problem in ceiling radiant cooling panels, J. Build. Eng. 32 (2020) 101707.

[22] H. Tang, X.-H. Liu, H. Li, et al., Study on the reduction of condensation risks on the radiant cooling ceiling with superhydrophobic treatment, Build. Environ. 100 (2016) 135–144.

[23] S.A. Mumma, Chilled ceilings in parallel with dedicated outdoor air systems: addressing the concerns of condensation, capacity, and cost, ASHRAE Trans. 108 (2) (2002) 220–231.

[24] C.L. Connroy, S.A. Mumma, Ceiling radiant cooling panels as a viable distributed parallel sensible cooling technology integrated with dedicated outdoor air systems, ASHRAE Trans. 107 (1) (2001) 578–585.

[25] G. Ge, F. Xiao, S. Wang, Neural network based prediction method for preventing condensation in chilled ceiling systems, Energy Build. 45 (2011) 290–298.

[26] S. Guo, Y. Tian, D. Fan, et al., A novel operating strategy to avoid dew condensation for displacement ventilation and chilled ceiling system, Appl. Therm. Eng. 176 (2020) 115344.

[27] I.-H. Yang, M.-S. Yeo, K.-W. Kim, Application of artificial neural network to predict the optimal start time for heating system in building, Energy Convers. Manag. 44 (17) (2003) 2791–2809.

[28] D. Xie, L. Tian, C.W. Yu, et al., Indoor thermal environment due to non-steady-state radiation heat transfer of a capillary ceiling radiation cooling system, Indoor Built Environ. 28 (4) (2019) 443–453.

[29] M.K. Kim, J. Liu, S.-J. Cao, Energy analysis of a hybrid radiant cooling system under hot and humid climates: a case study at Shanghai in China, Build. Environ. 137 (2018) 208–214.

[30] W. Jin, L. Jia, P. Gao, et al., The moisture content distribution of a room with radiant ceiling cooling and wall-attached jet system, Build. Simul. 10 (1) (2017) 41–50.

[31] J.H. Lim, J.H. Jo, Y.Y. Kim, et al., Application of the control methods for radiant floor cooling system in residential buildings, Build. Environ. 41 (1) (2006) 60–73.

[32] J. Ren, J. Liu, S. Zhou, et al., Experimental study on control strategies of radiant floor cooling system with direct-ground cooling source and displacement ventilation system: a case study in an office building, Energy 239 (2022) 122410.

[33] L.Z. Zhang, J.Z. Niu, Indoor humidity behaviors associated with decoupled cooling in hot and humid climates, Build. Environ. 38 (1) (2003) 99–107.

[34] J. Liu, S. Zhu, M. Kim, et al., A review of CFD analysis methods for personalized ventilation (PV) in indoor built environments, Sustainability 11 (15) (2019) 4166.

[35] J. Liu, J. Ren, L. Zhang, et al., Optimization of control strategies for the radiant floor cooling system combined with displacement ventilation: a case study of an office building in Jinan, China, Int. J. Archit. Eng. Technol. 6 (1) (2019) 33–48.

[36] Z. Kang, X. Peng, X. Cheng, et al., Analysis of condensation and thermal comfort of two kinds of compound radiant cooling air conditioning systems based on displacement ventilation, Procedia Eng. 205 (2017) 1529–1534.

[37] J. Liu, Z. Li, M.K. Kim, et al., A comparison of the thermal comfort performances of a radiation floor cooling system when combined with a range of ventilation systems, Indoor Built Environ. 29 (4) (2020) 527–542.

[38] H. Li, C. Xi, X. Kong, et al., A comparative experimental investigation on radiant floor heating system and stratum ventilation, Sustain. Cities Soc. 52 (2020) 101823.

[39] J. Liu, D.A. Dalgo, S. Zhu, et al., Performance analysis of a ductless personalized ventilation combined with radiant floor cooling system and displacement ventilation, Build. Simul. 12 (5) (2019) 905–919.

[40] L. Zhang, J. Liu, M. Heidarinejad, et al., A two-dimensional numerical analysis for thermal performance of an intermittently operated radiant floor heating system in a transient external climatic condition, Heat Transf. Eng. 41 (9–10) (2020) 825–839.

[41] M. Su, J. Liu, S. Zhou, et al., Dynamic prediction of the pre-dehumidification of a radiant floor cooling and displacement ventilation system based on CFD and a BP neural network: a case study of an office room, Indoor Built Environ. (2022) In press. doi: 10.1177/1420326x221107110.

[42] A. Al-Habaibeh, A. Sen, J. Chilton, Evaluation tool for the thermal performance of retrofitted buildings using an integrated approach of deep learning artificial neural networks and infrared thermography, Energy Built Environ. 2 (4) (2021) 345–365.

[43] A.E. Ruano, E.M. Crispim, E.Z.E. Conceic¸a~o, et al., Prediction of building's temperature using neural networks models, Energy Build. 38 (2006) 682–694.

[44] A.E. Ben-Nakhi, M.A. Mahmoud, Energy conservation in buildings through efficient A/C control using neural network, Appl. Energy 73 (2002) 5–23.

[45] A.E. Ben-Nakhi, M.A. Mahmoud, Cooling load prediction for buildings using general regression neural networks, Energy Convers. Manag. 45 (2004) 2127–2141.

[46] I.-H. Yang, K.-W. Kim, Prediction of the time of room air temperature descending for heating systems in buildings, Build. Environ. 39 (2004) 19–29.

[47] A. Keblawi, N. Ghaddar, K. Ghali, Model-based optimal supervisory control of chilled ceiling displacement ventilation system, Energy Build. 43 (6) (2011) 1359–1370.

[48] Sholahudin Nasruddin, P. Satrio, et al., Optimization of HVAC system energy consumption in a building using artificial neural network and multi-objective genetic algorithm, Sustain. Energy Technol. Assess. 35 (2019) 48–57.

[49] B. Karacavus, K. Aydin, Numerical investigation of general and local thermal comfort of an office equipped with radiant panels, Indoor Built Environ. 28 (6) (2019) 208–214.

[50] M.K. Kim, Y.S. Kim, J. Srebric, Impact of correlation of plug load data, occupancy rates and local weather conditions on electricity consumption in a building using four back-propagation neural network models, Sustain. Cities Soc. 62 (2020) 102321.

[51] W. Zhou, S. Xiong, Optimization of BP neural network classifier using genetic algorithm, Energy Procedia 11 (2011) 578–584.

[52] K. Horikiri, Y. Yao, J. Yao, Numerical study of unsteady airflow phenomena in a ventilated room, Comput. Therm. Sci. 4 (4) (2012) 317–333.

[53] K. Horikiri, Y. Yao, J. Yao, Modelling conjugate flow and heat transfer in a ventilated room for indoor thermal comfort assessment, Build. Environ. 77 (6) (2014) 135–147.

[54] GB 50365-2019Ministry of Housing and Urban-Rural Development of the People's Republic of China (MOHURD), China Architecture & Building press, Beijing, 2019.

[55] H. Skistad, E. Mundt, P.V. Nielsen, et al., Displacement ventilation in non-industrial premises, REHVAC: federation of European heating (2002).

[56] C. Zhang, M. Pomianowski, P.K. Heiselberg, et al., A review of integrated radiant heating/cooling with ventilation systems-Thermal comfort and indoor air quality, Energy Build. 223 (2020) 1–19.

[57] H. Xu, J. Niu, Numerical procedure for predicting annual energy consumption of the under-floor air distribution system, Energy Build. 38 (2006) 641–647.

[58] T. Zhang, Q. Hari, Q. Zhao, The use of the interval Pareto sorting method in simulation-based design of an indoor environment, Sci. Technol. Built Environ. 24 (2018) 410–417.

[59] X. Ma, X. Li, X. Shao, et al., An algorithm to predict the transient moisture distribution for wall condensation under a steady flow field, Build. Environ. 67 (2013) 56–68.

[60] M.K. Kim, B. Cremers, J. Liu, et al., Prediction and correlation analysis of ventilation performance in a residential building using artificial neural network models based on data-driven analysis, Sustain. Cities Soc. 83 (2022) 103981.

[61] S. Cao, S. Zhou, J. Liu, et al., Wood classification study based on thermal physical parameters with intelligent method of artificial neural networks, Bioresources 17 (1) (2022) 1187–1204.

[62] K. Vijayalakshmi, K. Vijayakumar, K. Nandhakumar, Prediction of virtual energy storage capacity of the air-conditioner using a stochastic gradient descent based artificial neural network, Electr. Power Syst. Res. 208 (2022) 107879.

[63] A. Qi, Research on prediction model of improved BP neural network optimized by genetic algorithm, 4th International Conference on Machinery, Materials and Computer, 2017.

[64] T. Liu, G. Zou, Evaluation of mechanical properties of materials based on genetic algorithm optimizing BP neural network, Comput. Intell. Neurosci. 2021 (2021) 2115653.

[65] W. Huang, H. Lam, Using genetic algorithms to optimize controller parameters for HVAC systems, Energy Build. 26 (3) (1997) 277–282.

ARTICLE IN PRESS

JID: ENBENV [m5GeSdc;September 7, 2022;18:55]

M. Su, J. Liu, M.K. Kim et al. Energy and Built Environment xxx (xxxx) xxx

[66] W. Wang, R. Zmeureanu, H. Rivar, Applying multi-objective genetic algorithms in green building design optimization—ScienceDirect, Build. Environ. 40 (11) (2005) 1512–1525.

[67] S.S. Arnas, G.N. Nasruddin, Optimization of a cascade refrigeration system using refrigerant C3H8 in high temperature circuits (HTC) and a mixture of C2H6/CO2 in low temperature circuits (LTC), Appl. Therm. Eng. 104 (2016) 96–103.

[68] N. Rajasekar, B. Jacob, K. Balasubramanian, et al., Comparative study of PEM fuel cell parameter extraction using genetic algorithm, Ain Shams Eng. J. 6 (4) (2015) 1187–1194.

[69] T. Zhang, Y. Liu, Y. Rao, et al., Optimal design of building environment with hybrid genetic algorithm, artificial neural network, multivariate regression analysis and fuzzy logic controller, Build. Environ. 175 (2020) 106810.

[70] X. Zhang, L. Sun, Optimization of optical machine structure by backpropagation neural network based on particle swarm optimization and Bayesian regularization algorithms, Materials (Basel) 14 (2021) 2998.

[71] V. Moyo, k. Sibanda, The generalization ability of artificial neural networks in forecasting TCP/IP traffic trends: how much does the size of learning rate matter? Int. J. Comput. Sci. Appl. 4 (1) (2015) 8–17.

[72] X. Wu, J. Shen, M. Wang, et al., Intelligent predictive control of large-scale solvent-based CO2 capture plant using artificial neural network and particle swarm optimization, Energy 196 (2020) 117070.

[73] Q.-q. Li, C. Chen, Y. Zhang, et al., Analytical solution for heat transfer in a multilayer floor of a radiant floor system, Build. Simul. 7 (3) (2014) 207–216.

[74] H. Jing, Z. Quan, R. Dong, et al., Performance simulation and optimization of new radiant floor heating based on micro heat pipe array, Build. Simul. 15 (2022) 1295–1308.

[75] S. Verbeke, A. Audenaert, Thermal inertia in buildings: a review of impacts across climate and building use, Renew. Sustain. Energy Rev. 82 (2018) 2300–2318.

[76] J. Ren, J. Liu, S. Zhou, et al., Developing a collaborative control strategy of a combined radiant floor cooling and ventilation system: a PMV-based model, J. Build. Eng. 54 (2022) 104648.

[77] D. QU, Research on enhanced generalization ability for the ANN's identification model, J. Naval Aeronaut. Eng. Inst. 22 (2007) 109–113.

[78] J. Ren, S.-J. Cao, Development of self-adaptive low-dimension ventilation models using OpenFOAM: towards the application of AI based on CFD data, Build. Environ. 171 (2020) 106671.